www.acsnano.oro

Multispectral Fingerprinting Resolves Dynamics of Nanomaterial Trafficking in Primary Endothelial Cells

Mitchell Gravely and Daniel Roxbury*



Downloaded via Daniel Roxbury on June 29, 2021 at 15:35:43 (UTC). See https://pubs.acs.org/sharingguidelines for options on how to legitimately share published articles.

Cite This: https://doi.org/10.1021/acsnano.1c04500



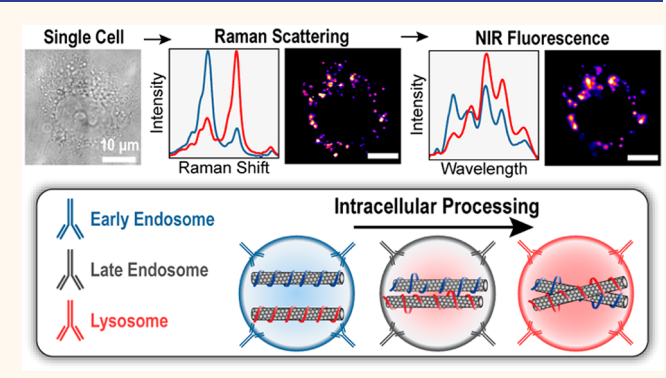
ACCESS

Metrics & More

Article Recommendations

Supporting Information

ABSTRACT: Intracellular vesicle trafficking involves a complex series of biological pathways used to sort, recycle, and degrade extracellular components, including engineered nanomaterials (ENMs) which gain cellular entry via active endocytic processes. A recent emphasis on routes of ENM uptake has established key physicochemical properties which direct certain mechanisms, yet relatively few studies have identified their effect on intracellular trafficking processes past entry and initial subcellular localization. Here, we developed and applied an approach where single-walled carbon nanotubes (SWCNTs) play a dual role—that of an ENM undergoing intracellular processing, in addition to functioning as the signal transduction element reporting these events in individual cells with single



organelle resolution. We used the exceptional optical properties exhibited by noncovalent hybrids of single-stranded DNA and SWCNTs (DNA-SWCNTs) to report the progression of intracellular processing events via two orthogonal hyperspectral imaging approaches of near-infrared (NIR) fluorescence and resonance Raman scattering. A positive correlation between fluorescence and G-band intensities was uncovered within single cells, while exciton energy transfer and eventual aggregation of DNA-SWCNTs were observed to scale with increasing time after internalization. An analysis pipeline was developed to colocalize and deconvolute the fluorescence and Raman spectra of subcellular regions of interest (ROIs), allowing for single-chirality component spectra to be obtained with submicron spatial resolution. This approach uncovered correlations between DNA-SWCNT concentration, dielectric modulation, and irreversible aggregation within single intracellular vesicles. An immunofluorescence assay was designed to directly observe the DNA-SWCNTs in labeled endosomal vesicles, revealing a distinct relationship between the physical state of organelle-bound DNA-SWCNTs and the dynamic luminal conditions during endosomal maturation processes. Finally, we trained a machine learning algorithm to predict endosome type using the Raman spectra of the vesicle-bound DNA-SWCNTs, enabling major components in the endocytic pathway to be simultaneously visualized using a single intracellular reporter.

KEYWORDS: intracellular trafficking, endosomal maturation, confocal Raman microscopy, hyperspectral imaging, near-infrared fluorescence, machine learning, immunofluorescence colocalization

INTRODUCTION

Intracellular trafficking is a highly regulated yet diverse system of pathways involving the entry, translocation, and localization of cargo internalized by endocytic cells.^{1–3} The endosomal maturation process, which initializes the main cellular degradation pathway, entails a dramatic series of physicochemical changes; a drop in luminal pH, influx of lysosomal enzymes, and change of ionic environment all promote digestion of vesicle contents.³ Most types of engineered nanomaterials (ENMs) gain cellular entry through active endocytic processes,⁴ where they are trafficked through these endosomal pathways before accumulating in lysosomal vesicles.^{5,6} The key mechanisms of

entry and localization of ENMs in biological systems have been extensively studied.⁷ The differential uptake of ENMs based on their size,⁸ shape,⁹ and surface chemistry¹⁰ has provided insight on targeting, while the formation of a protein corona on the

Received: May 27, 2021 Accepted: June 24, 2021



ENM surface is a dynamic process that can further direct biological interactions. 11,12 In contrast, the pathways that these ENMs are subject to after internalization, as well as the effects they might have on these pathways, lack the same depth of clarity despite the importance of these native processes. Proper lysosomal function and trafficking are essential in multiple metabolic pathways which regulate basic cellular functions including autophagy, nutrient degradation, and catabolite export. In addition, dysfunction of the endosomal-lysosomal pathways has been implicated in Alzheimer's disease, 13 lysosomal storage disorders, 14,15 and infectious diseases. 16 As EMNs are developed for biomedical applications, it is crucial to understand their environmental interactions in complex biological systems at the single-organelle level in order to properly assess their impact on key cellular functions. Intracellular trafficking is accurately described by a range of characteristics across a population of vesicles due to the asynchronous nature of the endocytic pathway,³ and thus cell-averaged analysis leads to systematic and compound errors. By tracking the fate of individual endosomal pathway reporters, a more accurate representation of the distribution of processes can be obtained to provide a deeper understanding of the dynamic ENM trafficking system.

The continuous evolution of endocytic vesicles presents a challenging system to investigate since experimental strategies are often limited by the optical capabilities of a given ENM. Fluorescence microscopy and organelle colocalization have routinely been used, providing valuable insight on the spatial and temporal localization of internalized ENMs; 17,18 however, traditional fluorophores lack environmental responsivity. Hyperspectral microscopy and confocal Raman imaging, which can both resolve spectral data with spatial resolution, are two approaches that can provide information about physical and chemical components within a system. Near-infrared (NIR) hyperspectral fluorescence imaging has enabled environmental sensing within endosomal vesicles of live cells, 5,19,20 while Raman probes have been designed to report intracellular aggregation, 21 pH, 22 as well as the molecular composition within various endosomal vesicles.²³ These approaches provide robust intracellular data which can characterize the complex ENM interactions in biological settings, however more suitable methods for processing and interpreting these highly dimensional data sets must be developed to enable widespread adoption of these techniques.²⁴

Single-walled carbon nanotubes (SWCNTs) are among the distinctive materials which exhibit both NIR fluorescence and resonance Raman scattering as intrinsic optical properties, 25 making them exceptional reporters of physical and environmental changes. The electronic structure of a given SWCNT, including its metallic or semiconducting character, ²⁶ is dependent on its chiral identity (denoted by the integers (n,m)), which varies by diameter and roll-up angle. Each chirality possesses distinct optical transition energies between valence and conduction bands (E_{ii} , where i = 1, 2, etc.),²⁷ and as a result, the intensity of the Raman spectrum from SWCNTs with E_{ii} resonant with the laser excitation is significantly enhanced by resonance Raman scattering.²⁸ At the same time, semiconducting SWCNTs exhibit band gap fluorescence when excited at their E_{22} resonances (500–900 nm);²⁹ however, the two observed spectra provide discrete information which can detail their physical state and local environment. The Raman spectrum contains multiple features, most notably the radial breathing mode (RBM, $150-350 \text{ cm}^{-1}$) and G-band (~1589 cm⁻¹),

which can be used to characterize the chiral composition, ²⁷ concentration, ³⁰ aggregation state, ³¹ and surface chemistry ³² of a SWCNT mixture. SWCNTs emit fluorescence in the NIR range (~900–1400 nm), where absorbance and scattering effects from biological samples are at a minimum, ³³ to produce a multipeak spectrum of all excitable chiralities at a given excitation wavelength. Because SWCNTs exhibit solvatochromism, ³⁴ the emission from each chirality is subject to position and intensity modulation in response to environmental changes, including analyte binding, ³⁵ changes in charge density, ³⁶ aggregation, ³⁷ pH, ²⁹ ionic environment, ³⁸ and reactive oxygen species. ³⁹

Single-stranded DNA, which can disperse single SWCNTs into a stable aqueous suspension, 40 provides a biocompatible surface functionalization while preserving their advantageous optical properties. 41,42 DNA-SWCNTs are internalized by cells via energy dependent endocytosis and are reported to localize to intracellular vesicles in the endolysosomal pathway, 5,19 making them exceptional candidates to nonspecifically target these trafficking processes. Therefore, we propose that simultaneous characterization of (1) the intracellular environmental conditions and (2) the ENMs physical condition can be achieved using DNA-SWCNTs, allowing for a multispectral characterization of the intracellular trafficking processes. Here, we report the internalization and intracellular processing of DNA-SWCNTs within individual primary endothelial cells using a dual-hyperspectral colocalization technique, which correlated intracellular fluorescence and Raman spectra. In tandem, the responsive NIR fluorescence and multifeatured Raman scattering from DNA-SWCNTs detail the changing intracellular environment and the resultant condition of the SWCNT hybrids in primary endothelial cells. We observed a temporal increase in local concentration of DNA-SWCNTs, inducing exciton energy transfer (EET)⁴³ and aggregation at two distinct rates within concentrated regions during intracellular processing. Pharmacological inhibitors of endosomal maturation effectively eliminated these events, confirming that these processes were responsible for the observed outcomes, while a DNA sequence dependence was generally not observed. Common regions of interests (ROIs) were identified within individual cells to colocalize the subcellular regions and spectral deconvolution was performed to obtain single-chirality component spectra. A relationship between concentration, aggregation, and NIR fluorescence modulation was identified within nanoscale regions, exhibiting heterogeneity which varied in time. These dynamic parameters were correlated to endosomal trafficking using an immunofluorescence assay to colocalize DNA-SWCNT Raman spectra with labeled endosomal organelles, delineating the temporal accumulation and aggregation within lysosomal vesicles. Finally, a machine learning algorithm was applied to identify endosomes and lysosomes based on the Raman spectrum of encapsulated DNA-SWCNTs, enabling the major components of the endocytic pathway to be simultaneously resolved within single cells.

RESULTS AND DISCUSSION

Co-dependence of Fluorescence and G-Band Intensities. To develop a spectral model of nanomaterial trafficking, we first identified two formulations of DNA–SWCNTs which were previously shown to induce differential cellular responses when internalized by macrophages as potential intracellular reporters.²⁰ HiPco SWCNTs were aqueously dispersed with (GT)₆ or (GT)₃₀ oligonucleotides *via* probe-tip sonication and

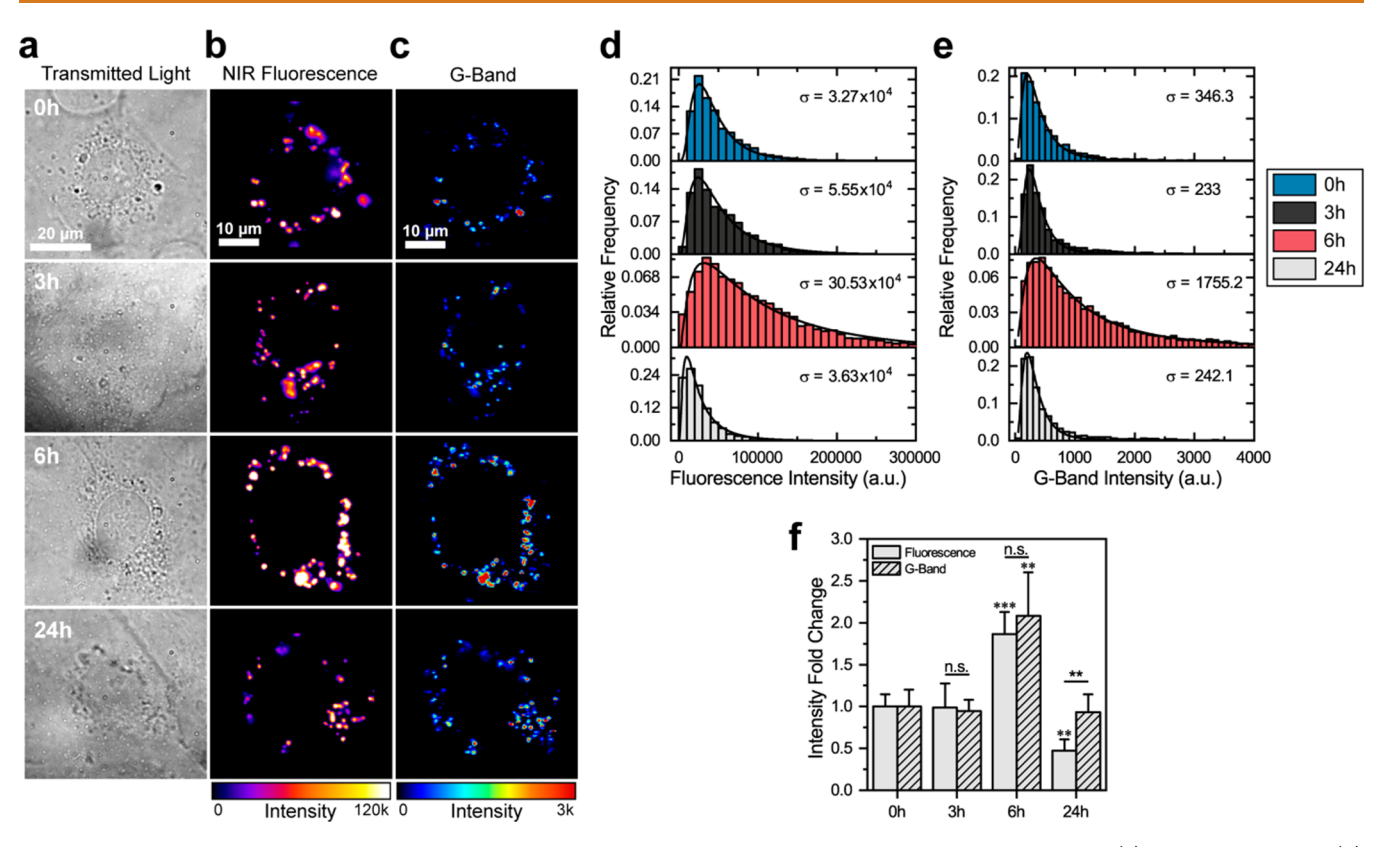


Figure 1. Fluorescence intensity and local concentration of DNA–SWCNTs are codependent within single cells. (a) Transmitted light, (b) broadband NIR fluorescence (950–1350 nm), and (c) G-band Raman intensity micrographs of individual cells dosed with 1 mg L⁻¹ (GT)₃₀ SWCNTs for 1 h and incubated in fresh media for indicated times. (d) Fluorescence intensity and (e) G-band intensity histograms of SWCNT-containing pixels from all examined cells at each time point. The distributions are fitted to log-normal curves, and the widths are estimated by the log standard deviation parameter (σ). (f) Fold change of average fluorescence and G-band intensities with respect to 0 h averages. Error bars represent mean \pm s.d. with $n \ge 4$ cells per condition. Five pointed stars between columns represent significance between fluorescence and G-band intensities and six pointed stars above columns represent significance *versus* 0 h values. (*p < 0.05, **p < 0.01, ***p < 0.001 according to two-tailed two-sample t test).

high-speed ultracentrifugation, resulting in highly purified, monodisperse DNA-SWCNT suspensions. 44 The presence of multiple peaks in both the visible and NIR range of their absorbance spectrum (Figure S1a) confirmed that both ssDNA sequences had suspended a multichiral mixture with strong optical absorbance. Excitation with a 730 nm laser produced bright fluorescence in the NIR range from multiple chiralities (Figure S1b), while the apparent differences in peak emission wavelengths were explained by the DNA sequence and nanotube chirality dependence on the hybrid structures.⁴⁵ A 1.58 eV (785 nm) laser source was used to acquire the Raman spectrum of both DNA-SWCNTs (Figure S1c,d), producing sharp peaks in both the radial breathing mode range (RBM, $150-350 \text{ cm}^{-1}$) and the G-band ($\sim 1589 \text{ cm}^{-1}$). Furthermore, the low intensity of the D-band (~1350 cm⁻¹) from both samples confirmed the removal of catalyst impurities and amorphous carbon from the raw HiPco materials. 40

Human umbilical vein endothelial cells (HUVEC primary cell line), a common *in vitro* model used to study neovascularization, 47 were chosen to represent the endothelium, which would contact any ENMs delivered through intravenous injection. First, HUVEC cultured in grid-labeled glass bottom Petri dishes were incubated with 1 mg-L $^{-1}$ of either (GT) $_{6^-}$ or (GT) $_{30^-}$ SWCNTs for 1 h under standard cell culture conditions, after which the SWCNT-containing media was removed and the cells were rinsed with phosphate-buffered saline (PBS). Next, the cells were either fixed with paraformaldehyde (considered the 0

h (hour) time point) or replenished with fresh media and allowed to incubate for additional time before fixation. Multiple cells from each condition, identifiable by their location within the grid-labeled culture area, were then imaged at 100× magnification using both NIR hyperspectral fluorescence and confocal Raman microscopes. Near identical images of the internalized DNA-SWCNTs were constructed from the broadband NIR fluorescence and G-band spectral regions (Figure 1a-c), each of which depicted distinct subcellular regions containing the $(GT)_{30}$ -SWCNTs. Histograms of the NIR fluorescence (Figure 1d) and G-band intensities (Figure 1e) were constructed using pixel values from the entire data set, revealing common temporal changes in the intensity distributions. To quantify these trends, the average intensity fold changes with respect to 0 h averages were computed (Figure 1f), showing nearly identical increases of fluorescence and G-band intensities at 6 h followed by differential reductions from 6 to 24 h. The G-band intensity, which is linearly dependent on SWCNT concentration, 30 could only increase over 6 h due to localized concentration increases in the cell, which we hypothesized could be due to fusion of intracellular vesicles over time. Moreover, we suspect the reduced fluorescence at 24 h could indicate an intracellular quenching mechanism such as DNA-SWCNT aggregation. Similar results were obtained from cells incubated with (GT)₆-SWCNTs throughout this study, indicating no clear dependence on DNA sequence. These results can be found in the Supporting Information.

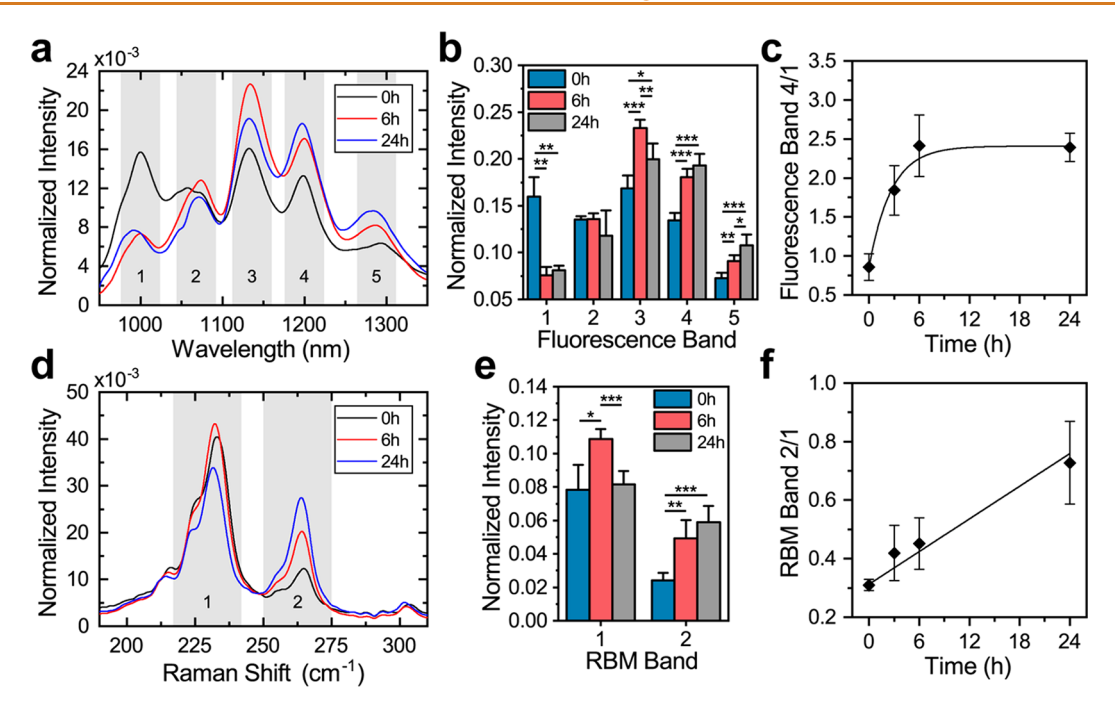


Figure 2. Temporal resolution of DNA–SWCNT spectral features indicates aggregation within subcellular regions. (a) Average fluorescence spectrum of $(GT)_{30}$ -SWCNTs in single cells after variable lengths of intracellular processing, normalized to the total integrated intensity of each spectrum. Fluorescence bands are indicated by shaded regions. (b) Average normalized fluorescence band intensities from $(GT)_{30}$ -SWCNTs in single cells after variable lengths of intracellular processing. Each spectrum was normalized by the total cell intensity, and average normalized band intensities are reported. (c) Ratiometric intensity of fluorescence band 4 divided by band 1, with exponential fit, as a function of time. (d) RBM region of the average Raman spectrum of $(GT)_{30}$ -SWCNTs in single cells after variable lengths of intracellular processing, normalized to the total integrated intensity of each spectrum. RBM bands are indicated by shaded regions. (e) Average normalized RBM band intensities from $(GT)_{30}$ -SWCNTs in single cells after variable lengths of intracellular processing. Each spectrum was normalized by the total cell RBM intensity, and average normalized band intensities are reported. (f) Ratiometric intensity of RBM band 2 divided by band 1, with linear fit, as a function of time. Error bars represent mean \pm s.d. for all, with $n \ge 4$ cells per condition. (*p < 0.05, **p < 0.01, ***p < 0.001 according to the two-tailed two-sample t test).

Spectral Features Identify Intracellular Aggregation of DNA-SWCNTs. While the broadband fluorescence intensity from DNA-SWCNTs is the integrated sum of all excited chiralities, the intensity from each individual chirality can be differentially affected. 45 By splitting the fluorescence spectrum from internalized DNA-SWCNTs into emission wavelength bands (Figure 2a), the integrated intensities corresponding to chiralities emitting over various wavelength windows could be quantified independently (Table S1).³⁶ The integrated intensity from each band was normalized by the total integrated intensity from each cell and the average normalized intensities were computed (Figure 2b), illustrating the relative intensity change of each band over time. We found that bands with lower emission energies (higher wavelength) generally increased over time, while the intensities of the two highest energy bands either decreased or remained constant, revealing certain chirality dependences. The ratiometric intensity of band 4 divided by band 1 (Figure 2c) provided a metric of this trend, which could be fitted to an exponential curve with respect to time. The decreasing and increasing of high and low energy emission intensities, respectively, are characteristics observed from exciton energy transfer (EET) between individual SWCNT chiralities in close proximity, ^{43,48} indicating a progressive degree of DNA-SWCNT flocculation occurring in time due to intracellular processing.

The same band deconvolution process was applied to the two dominant regions of the RBM spectrum (Figure 2d), and the average normalized intensities from cells at each time point were determined (Figure 2e), revealing a monotonic increase of band

2 with increasing incubation time. The ratiometric intensity of band 2 divided by band 1 (Figure 2f) quantified the intensity changes, displaying a linear increase in time. To explain these findings, we acquired Raman spectra of DNA-SWCNTs both in solution and aggregated out of solution (Figure S3) and identified the contributing chiralities present in each band along with their E_{22} transition energies when dispersed in a solution (Table S2).⁴⁹ In general, chiralities in band 1 were within the excitation resonance range of the 1.58 eV laser, resulting in higher intensity RBM features compared to band 2 when in solution. However, the dramatic increase of band 2 intensities upon aggregation is explained by a decrease in E_{22} transition energies, bringing these chiralities into resonance with the laser while simultaneously shifting band 1 chiralities out of resonance.³¹ Therefore, we attribute the increase of band 2 intensity over time to intracellular aggregation of DNA-SWCNTs, in agreement with previous findings,²¹ and propose the ratiometric intensity of band 2 divided by band 1 could be used to quantify the degree of aggregation. The fluorescence and RBM band ratios established could potentially discern between tightly compacted and irreversibly aggregated DNA-SWCNTs, respectively, due to their differing responses to complete SWCNT bundling. The fluorescence intensity of DNA-SWCNTs rapidly decreases upon formation of hard aggregates (i.e., direct contact between exposed SWCNT surfaces),⁵ eventually causing EET to reach a maximum level before becoming undetectable due to fluorescence quenching. In contrast, the RBM remains optically active regardless of dispersion quality, and thus a transition from closely packed

DNA—SWCNTs to directly aggregated SWCNT bundles could be identified as the point where fluorescence band 4/1 plateaus and RBM band 2/1 continues to increase.

Inhibition of Endosomal Maturation Reduces Spectral Changes. To confirm the observed spectral changes were induced via vesicle trafficking and endosomal maturation, we investigated the effect of inhibiting these native processes using two mechanistically different pharmacological inhibitors. HUVEC cells were incubated with DNA-SWCNTs following the same procedure previously described; however, the cells were treated with 10 μ g mL⁻¹ nocodazole (NOC), which polymerizes microtubules and inhibits vesicle motility,⁵² or 100 μM chloroquine (CQ), which elevates the luminal pH of endosomal vesicles, 53 for 6 h following DNA-SWCNT removal. The fold change of G-band and fluorescence intensities with respect to 0 h averages were computed for cells treated with both compounds (Figure 3a,b), revealing inhibited increases of G-band intensities from both treatments and a reduction of fluorescence from CQ-treated cells when compared to the 6 h control condition. We extended this analysis to examine the effect of pharmacological inhibition on intracellular EET and aggregation by calculating the fluorescence band 4 divided by band 1 intensity ratio (Figure 3c) and RBM band 2 divided by band 1 intensity ratio (Figure 3d). Significant inhibition of EET occurred from both treatments, while a high degree of variability in aggregation from individual cells was observed. Notably, the two treatments differentially affected the processes of intracellular trafficking and endosomal maturation, resulting in spectral similarities between 0 h or 3h untreated cells and 6 h CQ or NOC treated cells, respectively (Figure 3e,f). This could be explained by their differing mechanisms of action; CQ prevents endosomal maturation and vesicle fusion by directly inhibiting endosomal acidification,⁵⁴ while NOC does not inhibit the initial acidification of endosomes,⁵⁵ but rather prevents cargo from reaching and fusing with more acidic organelles. 52 This could allow the initial steps of vesicle maturation to occur during treatment with NOC, while initiation of these processes was immediately inhibited following treatment with CQ.

Segmentation and Colocalization of Intracellular **ROIs.** Spectra acquired within whole cells can provide ensemble measurements of internalized DNA-SWCNTs, yet the endocytic system is heterogeneous by nature due to a lack of synchrony between processes occurring simultaneously, potentially resulting in measurement bias toward more abundant processes while eliminating observation of rare occurrences within single vesicles.¹⁷ To overcome this issue, we developed a method which could segment a single cell into multiple regions of interest (ROIs) while colocalizing the signals from fluorescence and Raman spectra. First, NIR fluorescence and G-band intensity images (Figure 4a) were constructed, roughly colocalized, and binarized to create two equally sized template images. The template images were then segmented into separate matching ROIs (Figure 4b), which were individually confirmed and adjusted manually to account for processing errors and minor discrepancies in ROI locations. The pixels within each ROI were then averaged to create a single fluorescence and Raman spectrum belonging to each subcellular region (Figure 4c). Finally, the full fluorescence spectrum and the RBM of the Raman spectrum were deconvoluted to their chirality components using simultaneous multipeak fitting algorithms modeled by Voigt⁵⁶ and Lorentz⁵⁷ line shapes, respectively, while the G-band was fit independently to a single Lorentz curve. The fits were restricted by known peak

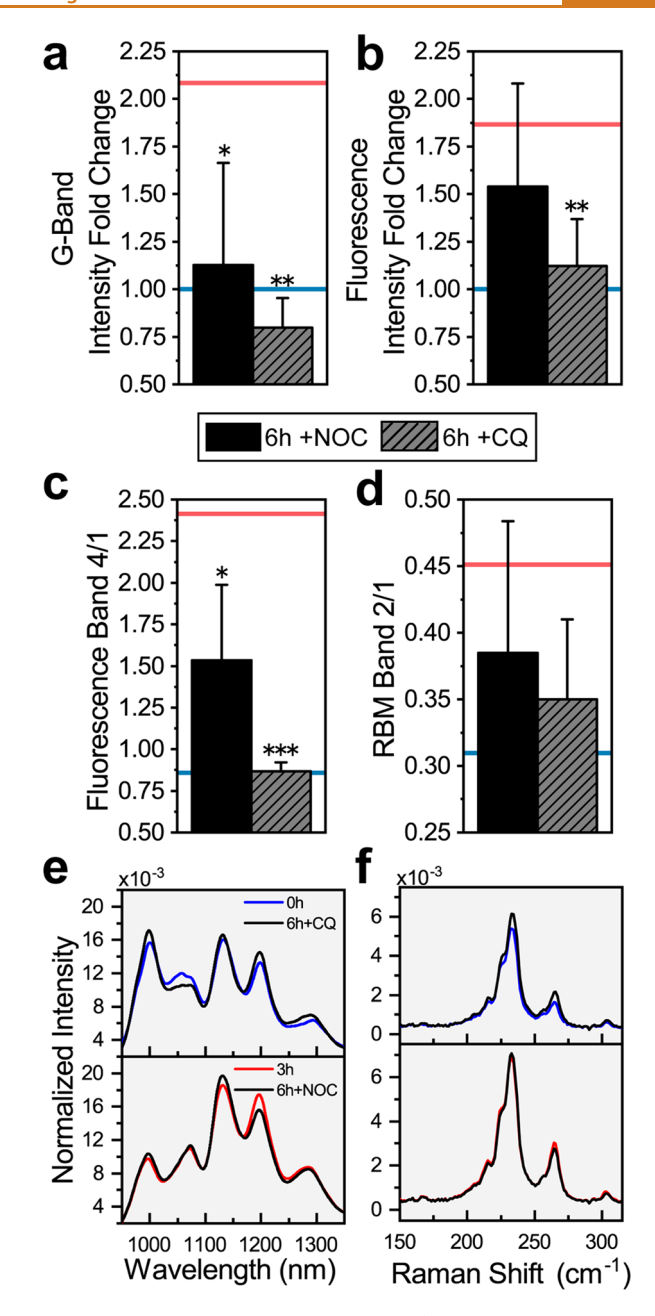


Figure 3. Spectral response to inhibition of endosomal progression. (a) Fold change of G-band and (b) fluorescence intensities, with respect to 0 h controls, from intracellular (GT)₃₀-SWCNTs after 6 h of incubation with nocodazole (NOC, $10~\mu \rm g~mL^{-1})$ or chloroquine (CQ, $100~\mu \rm M$). Averages from untreated cells at 0 or 6 h are shown as blue or red lines, respectively. (c) Ratiometric intensity of fluorescence band 4 divided by band 1 and (d) RBM band 2 divided by band 1 from inhibitor-treated cells after 6 h. Error bars represent mean \pm s.d. for all, with $n \geq 4$ cells per condition. Stars above error bars represent significance versus 6 h untreated cells. (*p < 0.05, **p < 0.01, ***p < 0.001 according to two-tailed two-sample t test). (e) Average intracellular fluorescence and (f) RBM spectra from inhibitor-treated cells after 6 h compared with spectra from untreated cells at indicated times. Each spectrum was normalized to the total integrated intensity.

characteristics from literature, ^{49,57} and the whole process was carefully monitored to avoid erroneous and overfitting of spectra.

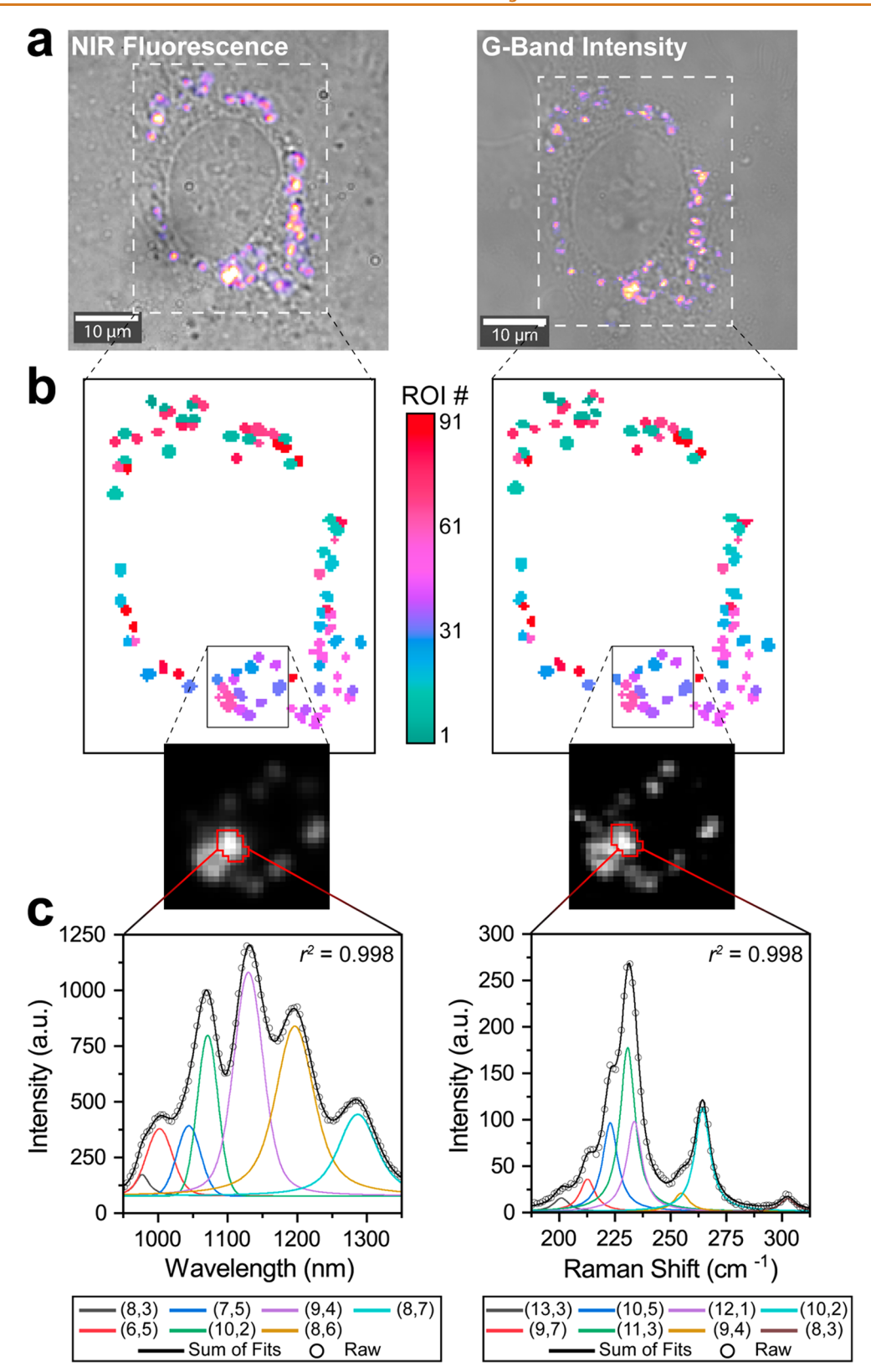


Figure 4. Colocalization of single-cell NIR fluorescence and Raman signals. (a) Transmitted light and brightfield images merged with broadband fluorescence and G-band intensity images, respectively, of a single cell incubated with DNA-SWCNTs. (b) Segmented ROI mask images determined from the fluorescence and G-band intensity images in (a). Inset shows magnified fluorescence and G-band intensity pixels corresponding to the outlined region in the masked image. (c) Deconvoluted fluorescence spectrum and RBM range of the Raman spectrum from the outlined cellular ROI in (b). Peaks from the fluorescence and RBM spectrum were fit to Voigt or Lorentz line shapes, respectively.

Fluorescence Modulation of Concentration Subcellular Regions. With the highly improved spatial resolution, we

first revisited the correlation between fluorescence intensity and G-band intensity using the colocalized subcellular ROIs. Figure

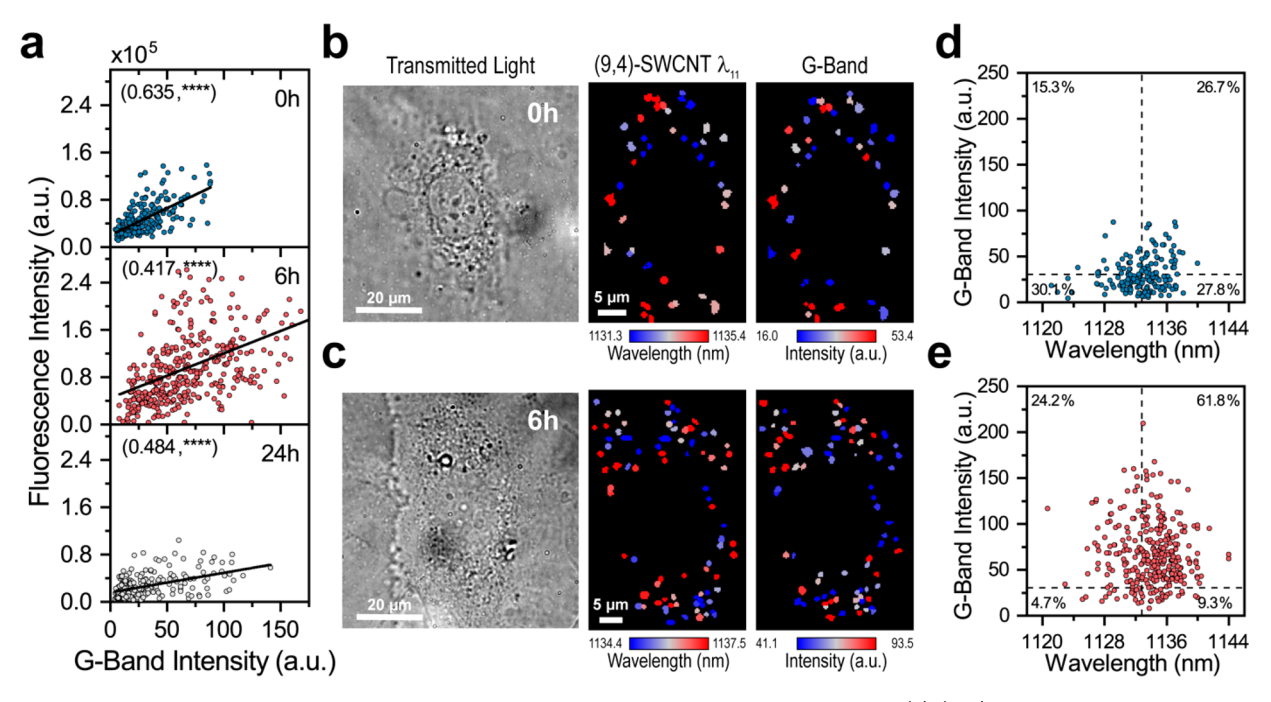


Figure 5. Fluorescence modulation from DNA–SWCNTs within concentrated subcellular regions. (a) $(GT)_{30}$ -SWCNT fluorescence intensity as a function of G-band intensity from all intracellular ROIs, with linear fits, at indicated time points. Pearson correlation coefficients, displayed in parentheses, were calculated from scatter data at each time point. (b) Transmitted light images, (9,4)-SWCNT emission maps, and G-band intensity maps of individual cells at 0 h or (c) 6 h time points. Color scale ranges encompass 20–80% of values from each ROI map. (d) G-band intensity as a function of (9,4)-SWCNT emission wavelength from all 0 h or (e) 6 h intracellular ROIs. Average values from 0 h data, represented as dashed lines, were used to compute the percent of ROIs in each quadrant.

Sa shows fluorescence intensity as a function of G-band intensity of all intracellular ROIs containing $(GT)_{30}$ -SWCNTs at various time points. A linear regression was performed, and the Pearson coefficient (r_p) was calculated for each data set, revealing a statistically significant positive correlation $(r_p > 0.4, p < 1e-4)$ at each time point. The sustained positive relationship between fluorescence intensity and DNA–SWCNT concentration confirmed a common mechanism could explain their temporal fluctuations, including the simultaneous increases observed from 0 h to 6 h. Since it is not possible for more DNA–SWCNTs to enter the cells after their initial dosing, we conclude that this is a signal of coalescence between vesicles of the endolysosomal pathway.

We next investigated the relationship between subcellular DNA-SWCNT concentration and fluorescence emission modulation. Hyperspectral maps of (9,4)-SWCNT emission wavelength and G-band intensity were constructed from the ROIs of cells imaged at 0 or 6 h (Figure 5b,c), revealing that redshifted regions were generally correlated to more concentrated areas regardless of incubation time. To quantify this trend, scatter plots were created to compare these two measurements from all ROIs at 0 or 6 h time points (Figure 5d,e). Average values from 0 h data were used to split the ROI population into four quadrants, thus providing a quantitative measure of their change due to intracellular processing events. The majority of DNA-SWCNT-containing ROIs had simultaneously redshifted and increased in concentration after 6 h; however, these shifts were completely prevented in cells treated with NOC or CQ (Figure S7), confirming the mechanism related to vesicle trafficking processes. The same trend was observed comparing the G-band intensity to (8,6)-SWCNT emission wavelength (Figure S9), revealing no apparent dependencies on SWCNT chirality. We partially attribute this correlation to the

formation of DNA–SWCNT-protein aggregates once the nanotube concentration reaches a certain threshold, in which densely packed proteins can increasingly perturb the DNA wrapping to increase solvent accessibility to the nanotube surface. This ultimately modulates the local dielectric environment, thus red shifting the SWCNT emission. At the same time, mature late endosomes and endolysosomes undergo a series of changes in their luminal environments, including a fluctuation of ion concentrations and an increase in negative surface charges, We surmise that a combination of these factors could be contributing to the observed ROI characteristics.

Intracellular Aggregate Formation Is Time Dependent. The RBM of a DNA-SWCNT Raman spectrum is directly related to the resonance of a chirality's transition energy with the excitation laser source. 28 In the case of SWCNT aggregation, a global decrease of transition energies causes distinctive changes to components of the RBM spectrum (Figure S11).31 More specifically, we observed that chiralities with $E_{22} < E_{laser}$ ($E_{22} >$ E_{laser}) displayed a substantial intensity decrease (increase) upon aggregation in control experiments (Figure S12a), providing a viable basis to probe the dynamics of intracellular aggregation using fitted RBM data (Figure 6a). To visualize the temporal progression of chirality components in all ROI spectra, we constructed a heat map illustrating the relative intracellular intensity change of each chirality with respect to solution intensities (Figure 6b) and included the aggregated controls as a reference. Each chirality was grouped based on its solution E_{22} value, revealing a clear trend as almost every chirality experienced an intensity change that suggested some amount of intracellular aggregation.

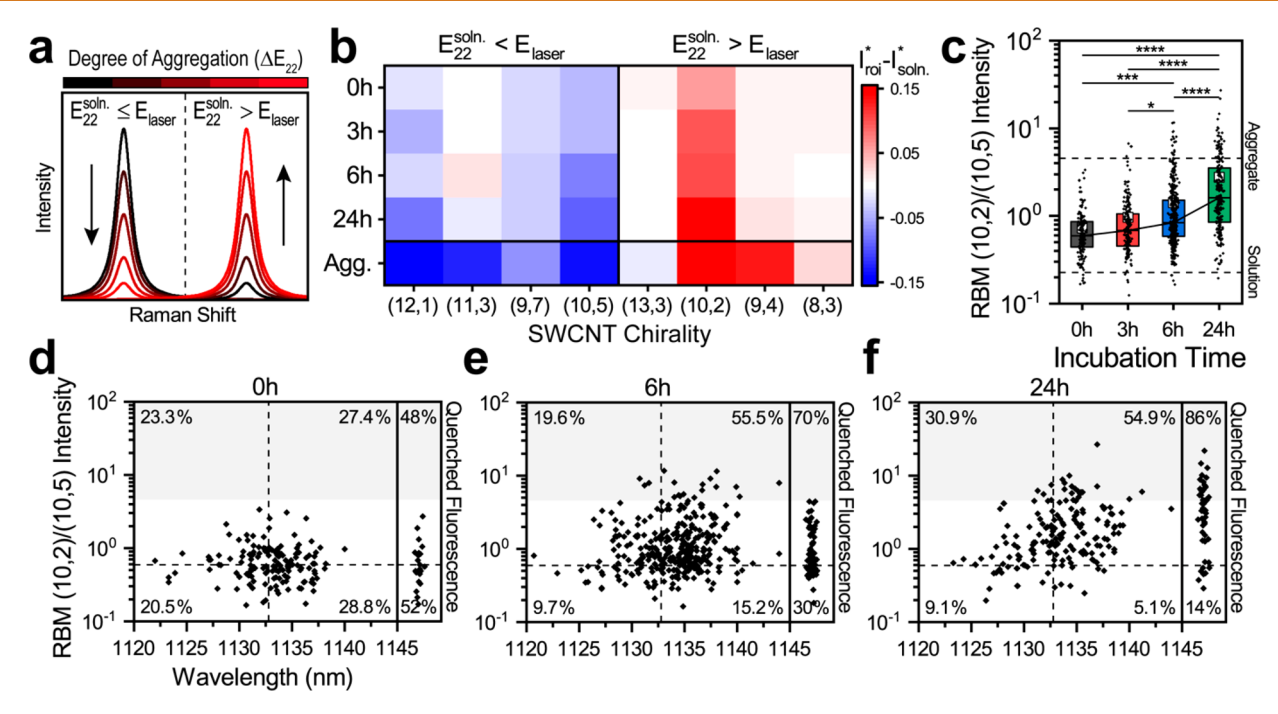


Figure 6. Intracellular aggregate formation is time dependent. (a) The RBM peak intensity of a single SWCNT depends on its transition energy (E_{22}) and the excitation energy (E_{laser}) . Aggregation shifts the optical transition to lower energies (ΔE_{22}) , resulting in selective intensity enhancement for chiralities brought into resonance $(E_{22}^{\text{soln}} > E_{\text{laser}})$ and intensity reduction for chiralities brought out of resonance $(E_{22}^{\text{soln}} > E_{\text{laser}})$ with the excitation. (b) Heat map representing the change of intracellular $(GT)_{30}$ -SWCNT RBM intensities from solution as a function of chirality and time. Control intensities of intentionally aggregated $(GT)_{30}$ -SWCNTs are displayed as a reference. The chirality intensities from each ROI or control replicate were normalized by the total RBM intensity and average values are reported. (c) The ratio of RBM (10,2)/(10,5) intensities of all intracellular ROIs as a function of time. Boxes represent 25–75% of the data, white squares represent means, trend lines connect medians, and dashed lines indicate values from aggregated or solution controls. One-way ANOVA with Tukey post hoc analysis was performed (*p < 0.05, **p < 0.01, ***p < 0.001, ****p < 1e-4). The ratio of RBM (10,2)/(10,5) intensities as a function of (9,4)-SWCNT emission wavelength of all (d) 0 h, (e) 6 h, or (f) 24 h ROIs. Boxed column scatter plots on the right-hand side depict RBM ratio values from ROIs with poorly fitting or quenched fluorescence. Median values from 0 h data, represented as dashed lines, were used to compute the percent of ROIs in each quadrant. Shaded regions indicate the RBM (10,2)/(10,5) intensity threshold identified from aggregated controls.

Next, we devised an intracellular aggregation measurement based on the RBM intensity changes observed upon SWCNT aggregation. We identified the ratiometric RBM intensity of (10,2)/(10,5) as a suitable metric for a number of reasons: (1) distinguishable RBM peaks from both chiralities are present in aggregated and solution controls, (2) the E_{22} of (10,5)-SWCNTs in solution (~1.58 eV) is directly in resonance with the laser and can only decrease with aggregate formation, and (3) the E_{22} of (10,2)-SWCNTs in solution (~1.69 eV) is greater than the laser energy and would move into resonance upon aggregate formation; however, the expected shift (\sim 70 meV)⁵⁹ due to complete bundling could not decrease the transition below the laser energy. Therefore, the RBM (10,2)/(10,5) intensity ratio (hereby referred to as the "RBM aggregate ratio") could directly relate chirality intensities to their transition energies to provide a quantitative measure of aggregation. Significantly different values of the RBM aggregate ratio were calculated from DNA-SWCNT controls of solution and aggregated spectra (Figure S12b), providing reference points to compare against the cellular data. The RBM aggregate ratio was then calculated for every intracellular ROI containing (GT)₃₀-SWCNTs and box plots were constructed for the full data set (Figure 6c), revealing significant differences between the distributions which increased and broadened in time. We then investigated whether a relationship could be identified between the degree of aggregation, environmental conditions within ROIs, and time of DNA-SWCNT processing within the

cells. Scatter plots of the RBM aggregate ratio as a function of (9,4)-SWCNT emission wavelength were constructed from ROIs after 0, 6, or 24 h of incubation with internalized $(GT)_{30}$ SWCNTs (Figure 6d-f). Each set of ROIs were split into four populations based on median values from 0 h data. The percentage of ROIs with red-shifted and increased RBM ratios effectively doubled from 0 h to 6 h, yet this number plateaued with additional incubation time. At the same time, an increasing number of ROIs became quenched over time (Figure S13). The majority of quenched ROIs, however, exhibited substantial aggregation, as shown in the right-hand column scatter plots of each time point. These spectral characteristics could be indicative of increasingly harsh environmental conditions which the DNA-SWCNTs were subjected to during later stages in the processing pathway, as evidenced by sequential red shifting, aggregate formation, and fluorescence quenching due to excessive aggregation. 50,51

Immunofluorescence Colocalization Identifies Dynamics of Intracellular Trafficking. To corroborate the observed spectral changes with specific organelles from the endosomal pathway, we devised an immunofluorescence assay to colocalize fluorescent antibody markers with Raman spectra from intracellular DNA–SWCNTs. We identified four specific protein markers to distinguish key intracellular compartments using fluorescent antibody labels. These protein markers included early endosome antigen 1 (EEA1), Ras-related proteins 7 and 11a (RAB7, RAB11a), and lysosomal-associated

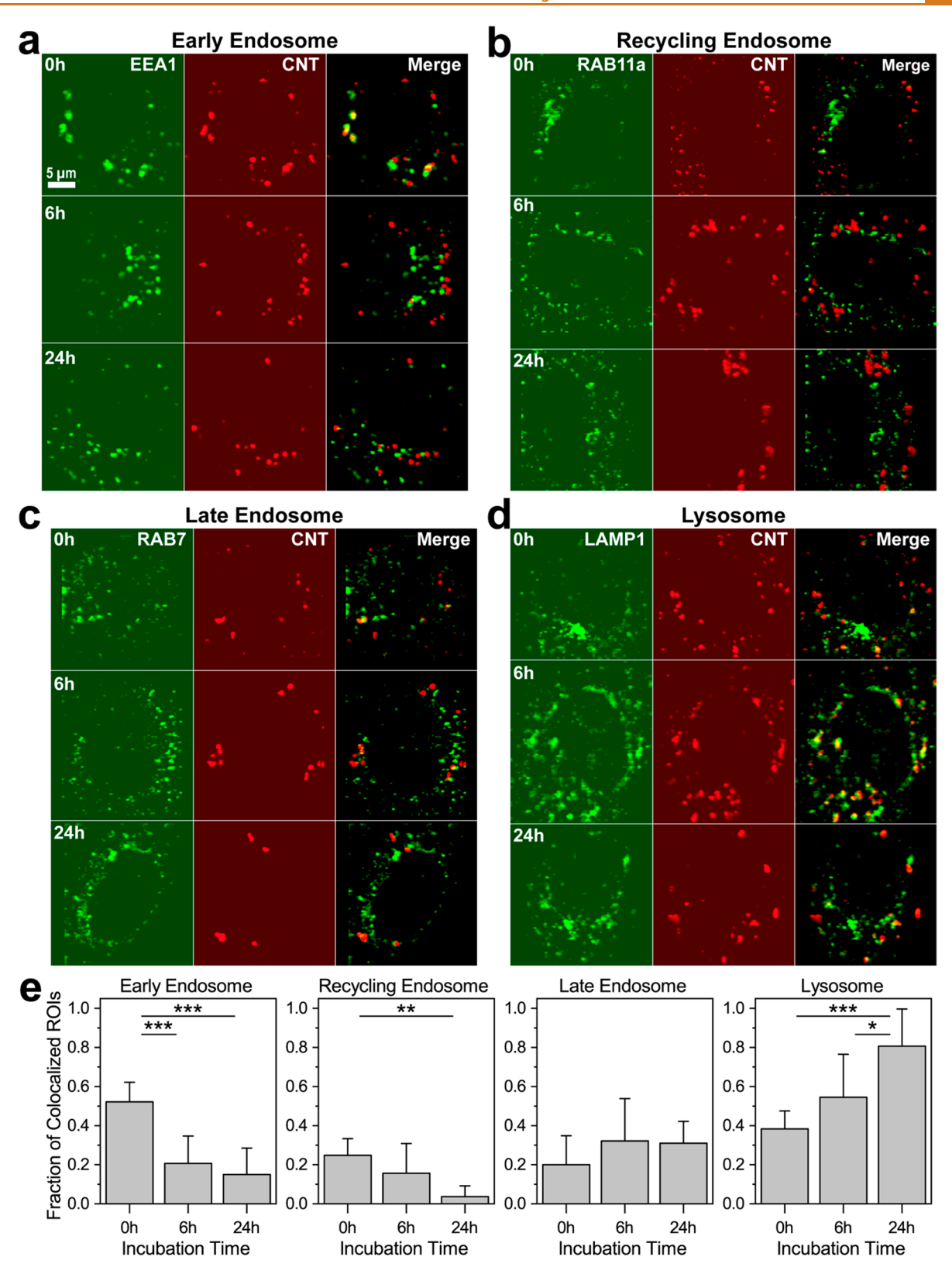


Figure 7. Immunofluorescence identifies dynamics of endosomal trafficking. Fluorescence images of cells labeled with (a) EEA1 (early endosome), (b) RAB11a (recycling endosome), (c) RAB7 (late endosome), or (d) LAMP1 (lysosome) antibody markers. Left panels (green) show immunofluorescence markers, middle panels (red) show Raman maps of $(GT)_{30}$ -SWCNTs, and right panels show the overlay. (e) Average fraction of SWCNT ROIs colocalized with each vesicle marker with respect to incubation time. Error bars represent mean \pm s.d. for all, with n=7 cells per condition. One-way ANOVA with Tukey post hoc analysis was performed (*p < 0.05, **p < 0.01, ***p < 0.001).

I

membrane protein 1 (LAMP1), which corresponded to early endosomes, ⁶⁰ late endosomes, ⁶¹ recycling endosomes, ⁶² and

lysosomes, 63 respectively. HUVEC cells which had been incubated with $(GT)_{30}$ -SWCNTs in the same method

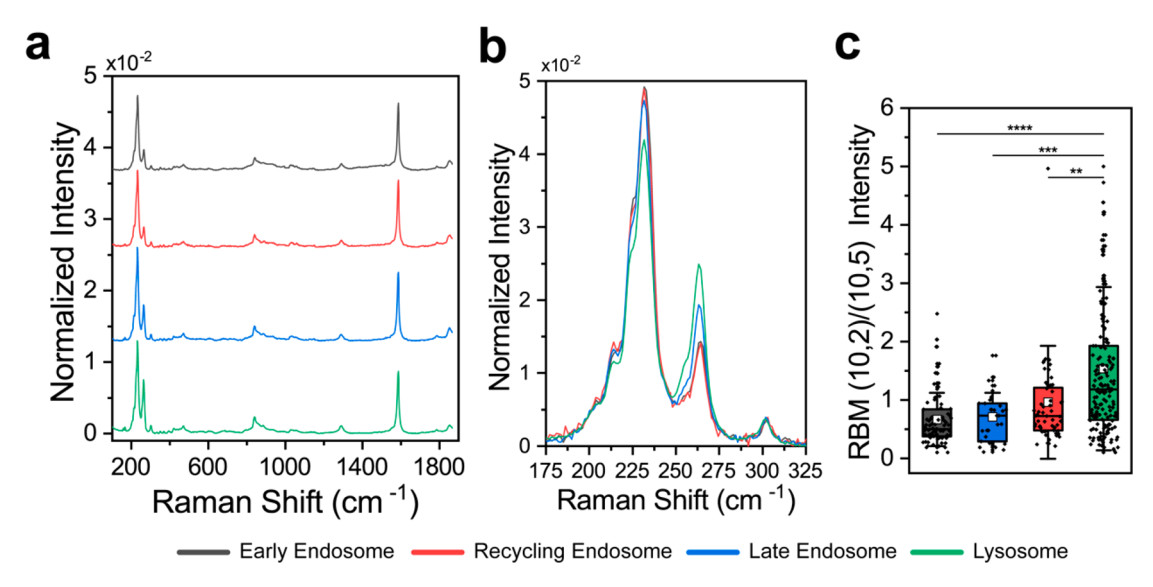


Figure 8. DNA—SWCNTs aggregate within lysosomes. (a) Average Raman spectrum and (b) RBM spectrum of $(GT)_{30}$ -SWCNTs colocalized with endosomal markers. Each spectrum was normalized by the total integrated intensity. (c) Ratio of RBM (10,2)/(10,5) intensities of all ROIs colocalized with endosomal markers. Boxes represent 25–75% of the data, white squares represent means, black line represents the median, and whiskers represent mean \pm s.d. One-way ANOVA with Tukey post hoc analysis was performed (*p < 0.05, **p < 0.01, ****p < 0.001, ****p < 1e-4).

previously described were fixed, labeled with one of four organelle markers, stained with a fluorophore-conjugated secondary antibody, and imaged with a confocal Raman microscope. Antibody fluorescence was collected by scanning single-cell areas using a low power (10 μ W) 532 nm laser excitation source. Although DNA-SWCNTs produce distinct Raman spectra using a 10 mW 532 nm excitation source, control experiments confirmed that the reduced laser power used to acquire fluorescence data could not produce detectable Raman scattering (Figure S15). Next, the sample area was rescanned using a 785 nm laser excitation source to collect hyperspectral Raman maps from the intracellular DNA-SWCNTs within the same area. The immunofluorescence data, generated as a 3D hyperspectral cube, was converted into a confocal fluorescence image by integrating along the spectral dimension, while the corresponding Raman intensity image was produced by integrating the RBM range of the spectral dimension (Figure

Parts a-d of Figure 7 show representative images of antibody fluorescence intensity, DNA-SWCNT Raman intensity, and merged two-channel images for each investigated condition. Early endosomes and lysosomes appeared to colocalize with the DNA-SWCNTs the most at initial and later time points, respectively, while little colocalization was observed with recycling and late endosomes. To quantify the degree of colocalization between images, we applied a global series of image processing techniques (see the Methods for details) to each set of antibody fluorescence or Raman images to create binary representations of the intracellular vesicles and internalized DNA-SWCNTs (Figure S17). The binary images of DNA-SWCNTs were then split into individual ROIs, and the fraction of ROIs which colocalized with the immunofluorescence labels was determined for each cell after various incubation times (Figure 7e). We note that the total fraction of colocalized ROIs exceeded 1 by varying amounts at each time point, however this could be interpreted as partial overlap between the different endosomal markers. 18,64 Trends were most apparent among early endosomes and lysosomes, in which

the fraction of colocalized ROIs monotonically decreased or increased with incubation time, respectively. Small amounts of DNA-SWCNTs colocalized with late endosomes throughout all time points, while recycling endosomes did not appear to play a major role in these processes at any time point. ROI colocalization with lysosomes significantly increased over a 24 h incubation time, after which ~80% of all nanotube ROIs were contained within lysosomal organelles. These findings corroborate with previous reports^{5,19} to confirm that DNA-SWCNTs progress through the endosomal pathway before accumulating within lysosomal vesicles. Additionally, we have previously shown that a fraction of DNA-SWCNTs can be released by a cell to the surrounding media through lysosome-mediated exocytosis,²⁰ a process in which a lysosome fuses with the plasma membrane to release its contents. The presence of DNA-SWCNTs in early endosomes after 24 h could be an indication that small amounts of DNA-SWCNTs were released from a cell and subsequently re-endocytosed.

The Lysosomal Environment Induces DNA-SWCNT **Aggregation.** Next, we extended the colocalization analysis to directly observe the full Raman spectrum from DNA-SWCNTs contained in labeled organelles. For each endosomal marker, we pooled the Raman spectrum from every immunofluorescencelabeled ROI to compare the average and population characteristics. The average Raman spectrum from each set of colocalized ROIs is shown in Figure 8a. Differences between spectra were most apparent in the RBM region (Figure 8b), which exhibited sequentially increasing high wavenumber peak intensities as the endocytic vesicle type progressed from early/recycling endosomes to late endosomes and lysosomes. To quantify these changes in the entire ROI population, we calculated the RBM aggregate ratio of each ROI and constructed a box plot to show aggregation as a function of vesicle type (Figure 8c). The RBM aggregate ratio was relatively constant between the early/ recycling/late endosomes, however a clear and statistically significant increase in aggregation occurred once the DNA-SWCNTs progressed to the lysosomes. Notably, the G-band intensity was mostly unaffected by vesicle type, increasing

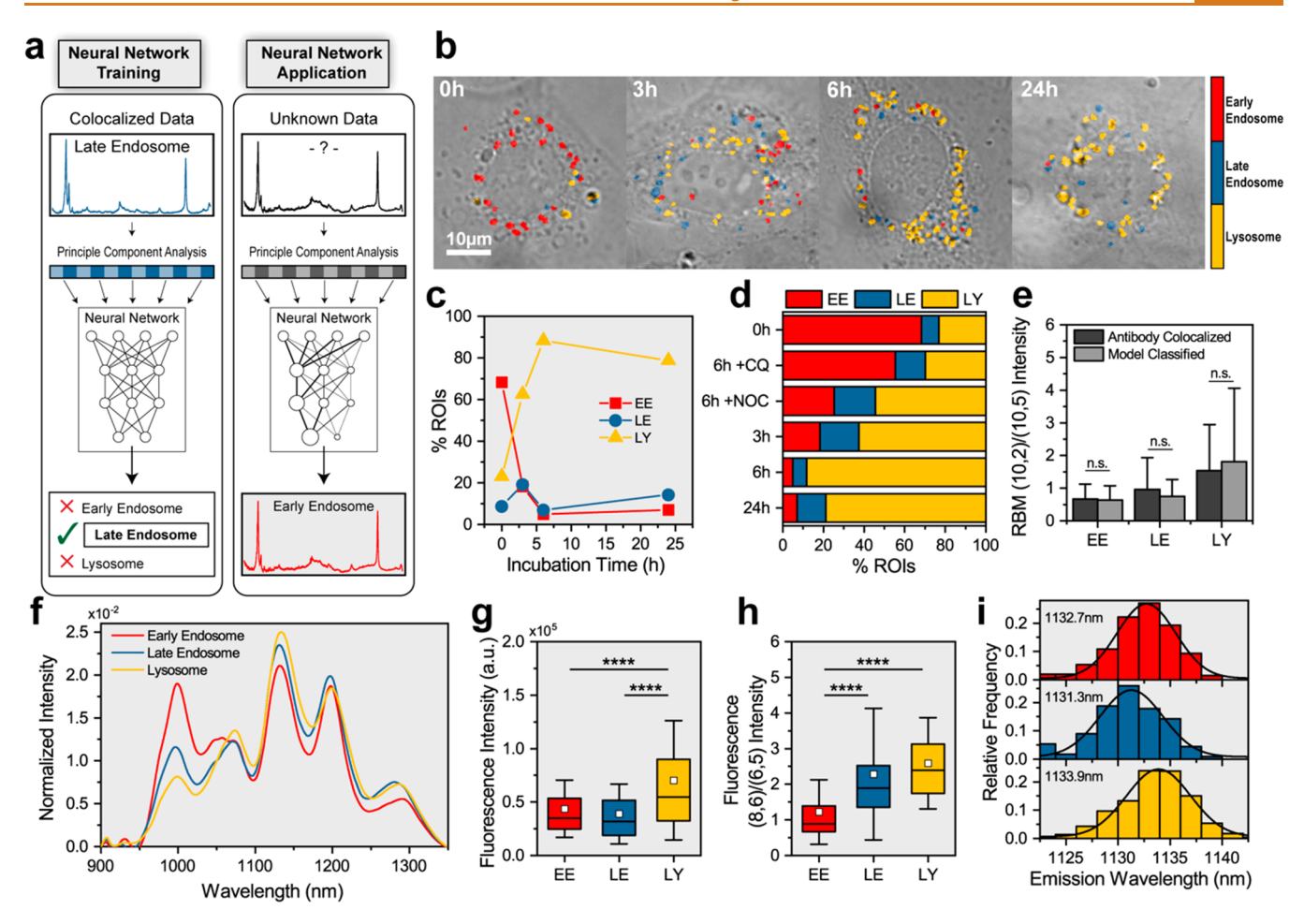


Figure 9. Machine learning facilitates endosomal mapping via DNA-SWCNT Raman spectra. (a) Schematic depicting the general process of building and applying an artificial neural network. Full Raman spectra from ROIs colocalized with endosomal markers were preprocessed by principle component analysis (PCA) and input to the untrained neural network (left) to establish and connect weighted variables to differentiate input classes. Next, the unknown data set was preprocessed, input to the trained neural network (right), and categorized to the vesicle type with the highest classification probability. (b) Endosomal maps overlaid on transmitted light images of single cells at various time points, depicting the predicted ROI class output from the artificial neural network. (c) Percent of ROIs categorized as early endosomes (EE), late endosomes (LE), or lysosomes (LY) as a function of time. (d) Stacked bar graph showing the percent of ROIs categorized as each vesicle type. (e) Average RBM (10,2)/(10,5) intensity of endosomal vesicles from immunofluorescence-labeled spectra and model-classified spectra. A two-tailed two-sample t test was performed between groups to determine significance (p > 0.05 for all). (f) Average fluorescence spectrum of each predicted vesicle type, normalized by the total intensity. Box plots depicting (g) integrated fluorescence intensity and (h) fluorescence (8,6)/(6,5) intensity from model-classified ROIs. Boxes represent 25-75% of the data, white squares represent means, black lines represent medians, and whiskers represent mean \pm s.d. One-way ANOVA with Tukey post hoc analysis was performed (*p < 0.05, **p < 0.01, ***p < 0.001, ****p < 0.001, ***p < 0.00

instead with the overall incubation time (Figure S18). These findings delineate lysosomes as the final intracellular destination for DNA-SWCNTs, where the catabolic environmental conditions promote irreversible bundling between nanotube surfaces. Moreover, the concentration of DNA-SWCNTs within the lysosomes does not appear to contribute to this type of direct-contact aggregation.

Endosomal Mapping via DNA-SWCNT Intracellular Reporters. In addition to the RBM changes displayed in Figure 8b, a number of minor but clear differences could be identified between various Raman features of immunofluorescencelabeled DNA-SWCNTs (Figure S19). We speculated that the distinct Raman profiles obtained from each type of organelle could act as their spectral marker, enabling classes of endosomal vesicle to be identified by the encapsulated DNA-SWCNTs. To investigate this concept, we implemented an artificial neural

network (ANN), a machine learning algorithm with exceptional performance in data classification and pattern recognition applications.⁶⁵ Using the Raman spectra of immunofluorescence-labeled ROIs as the training data set (see the Methods for details), the model was built to recognize early endosomes, late endosomes, and lysosomes based on the DNA-SWCNT Raman spectrum of an input ROI (Figure 9a). The model was validated with a 10-fold cross-validation and performance was assessed from the resulting confusion matrix and receiver operating characteristic (ROC) curves (Figure S20, Table S3), suggesting the ability to identify vesicle localization with an accuracy of over 84%. The model was then applied to classify the intracellular localization of the nonlabeled data set of (GT)₃₀-SWCNT ROIs using the Raman spectrum as the input variable. Endosomal maps were constructed by coloring each ROI by vesicle classification (Figure 9b), enabling simultaneous

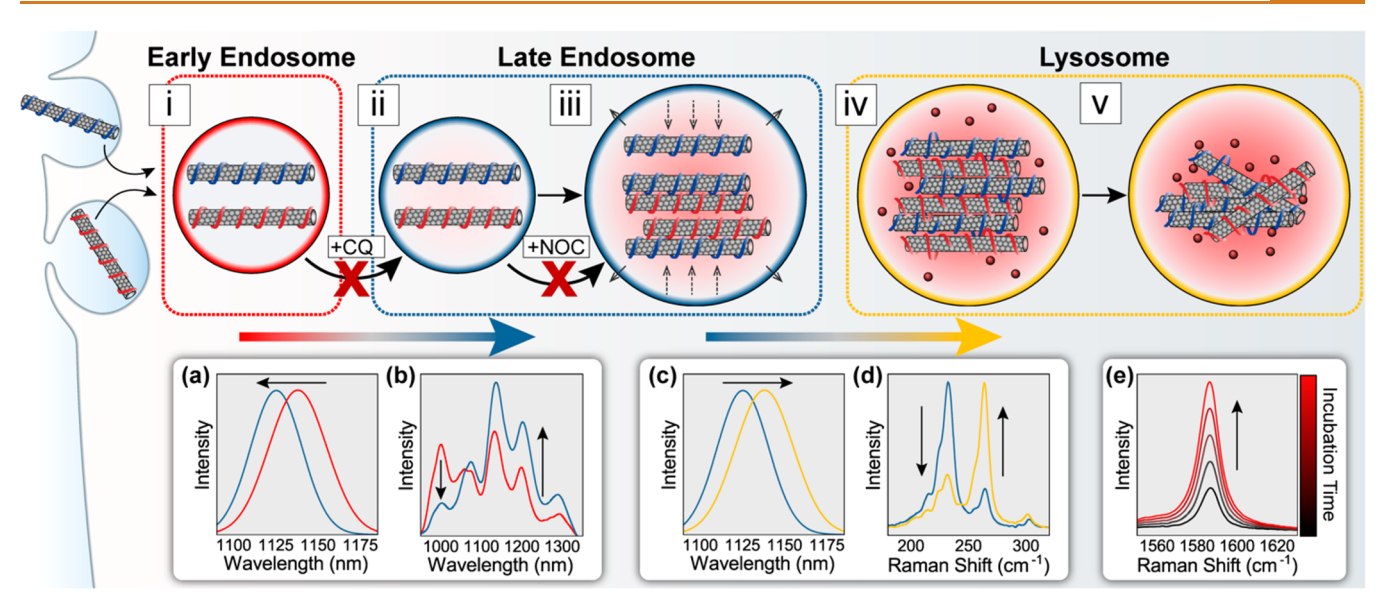


Figure 10. Schematic summarizing DNA-SWCNT trafficking through the endosomal pathway. (i-v) Depiction of sequential steps of DNA-SWCNT intracellular processing and (a-e) the identifiable spectral changes resulting from these processes.

resolution of DNA-SWCNT localization through key stages of the endosomal trafficking pathway. The percent of ROIs classified to each vesicle type was calculated for ROI populations with respect to time (Figure 9c), showing trends similar to those observed in Figure 7e. Additionally, a bar chart was constructed to summarize ROI classification for all conditions examined (Figure 9d). Notably, the classification of ROIs from cells dosed with CQ and NOC most closely resembled 0 and 3 h untreated populations, respectively, corroborating with the observations from Figure 3e,f. To confirm that characteristics from the modelclassified ROIs matched the original immunofluorescencelabeled data, the average RBM ratio was compared between each type of vesicle (Figure 9e). Similar values were obtained for each endosomal marker, suggesting the model had predicted the same characteristics identified from the immunofluorescencelabeled data.

Next, the SWCNT fluorescence characteristics of modelclassified ROIs were examined. The average NIR fluorescence spectrum from ROIs assigned to each endosomal marker exhibited distinct features (Figure 9f), suggesting the DNA-SWCNTs were responsive to the dynamic environmental conditions. Several fluorescence characteristics were identified and compared to elucidate the environmental differences between endosomal vesicles. The integrated fluorescence intensity was observed to remain constant between early and late endosomes before significantly increasing within the lysosomes (Figure 9g). Chirality-dependent intensity changes, specifically the intensity decrease (increase) of low (high) wavelength peaks, were quantified using the ratio of fluorescence (8,6)/(6,5) fitted peak intensities (Figure 9h). The ratiometric intensity progressively increased in each sequential endosomal vesicle, with mean values from early endosomes being significantly lower than late endosomes and lysosomes. Histograms of the (9,4)-SWCNT emission wavelength were fitted to Gaussian distributions to assess the differences in dielectric environment (Figure 9i). Relative to the emission wavelength of early endosomes, a blue-shift and a red-shift was identified from late endosomes and lysosomes, respectively.

Although the trend between vesicles varied considerably across the examined fluorescence characteristics, these observa-

tions could be explained by a combination of physical and environmental factors. To provide additional context, the same fluorescence properties were calculated from control fluorescence spectra of (GT)₃₀-SWCNTs acquired in a series of biologically relevant conditions, namely varying pH, salt concentration, and protein corona (Figures S21 and S22). A heat map was constructed to summarize these effects with respect to stock DNA-SWCNT conditions (Figure S23). Lysosome-classified ROIs exhibited the highest fluorescence intensities and fluorescence (8,6)/(6,5) intensities. Compared to early and late endosomes, the lysosomal lumen possesses high concentrations of Ca²⁺ along with an abundance of enzymes, other proteins, and amino acid catabolites, 66,67 all of which could promote these intensity changes. In addition, the ratiometric (8,6)/(6,5) intensity is responsive to exciton energy transfer (EET) between adjacent DNA-SWCNTs; hence, lysosomal aggregation can contribute to the high ratiometric intensities. On average, the emission wavelengths from (9,4)-SWCNTs were also the longest (red-shifted compared to early endosomes) in lysosome-classified ROIs. While the luminal pH (~4.5) caused a blue-shift of (9,4)-SWCNT emission wavelength in control experiments, we hypothesize that other lysosomal components preferentially interact with the DNA wrapping, thus controlling the local dielectric and red-shifting the fluorescence emission. For example, the presence of divalent cations, amphiphilic proteins, lipids, and charged residues could strongly interact with DNA-SWCNTs and prevent the effects of lowered pH. Late endosome-classified ROIs also exhibited significantly higher fluorescence (8,6)/(6,5) intensity ratios than early endosomes, however the average emission wavelength from (9,4)-SWCNTs was blue-shifted by ~1.4 nm. Since late endosomes are derived from the vacuolar domains of early endosomes, concentrated levels of endocytosed proteins are selectively retained from the tubular endosome structure, ⁶⁴ thus DNA-SWCNT-protein interactions could increase the fluorescence (8,6)/(6,5) intensity. At the same time, the rapid drop in pH upon late endosome formation in the absence of interactive lysosomal components could explain the blue-shift observed from late endosome-classified DNA-SWCNTs.

To illustrate these findings in terms of sequential trafficking events, we propose a schematic (Figure 10) to describe the intracellular processes which ultimately control the fate of internalized nanomaterials. An emphasis is placed on the endosomal maturation process, in which a highly coordinated series of events dramatically transform the endosomal vesicles, thus altering their physicochemical properties and controlling the luminal environment.³ The DNA-SWCNTs first enter the cell through active endocytic processes (i), where they are transported into early endosomes along with a cohort of endocytic cargo. Continuous recycling of transport vesicles sends the majority of internalized cargo back to the plasma membrane, however DNA-SWCNTs are retained by the early endosome to be included in the degradation pathway. Conversion into a late endosome is followed by a rapid decrease in luminal pH (ii), thus initiating the endosomal maturation process. Next, the encapsulated DNA-SWCNTs experience a coordinated series of physicochemical transformations (iii), including luminal acidification, ion flux across the endosomal membrane, and changes in size and morphology. DNA-SWCNTs identify late endosome containment with blue-shifted fluorescence emission (a) and chirality-dependent intensity modulation (b), while temporal fusion of DNA-SWCNTcontaining vesicles drives an increase in luminal nanotube concentrations (e). Acidification continues until lysosomal proteins, hydrolases, and other components are activated, eventually transforming the late endosome into a lysosome (iv). Here, the components of lysosomal environment bind to and interact with the DNA wrapping, promoting increasingly complex interactions between the DNA-SWCNTs and luminal biomolecules to ultimately modulate the dielectric environment and induce a red shift of DNA-SWCNT fluorescence emission (c). After a period of time in the lysosomes (v), internalized DNA-SWCNTs aggregate (d) and NIR fluorescence emission is quenched, marking the end of the trafficking pathway. In contrast, pharmacological inhibition of endosome maturation effectively suppresses these key spectral changes by preventing endosome acidification (CQ) or physically obstructing progression (NOC) by reducing endosome motility.

CONCLUSIONS

Herein, we developed a correlative approach to simultaneously study the intracellular fate of internalized nanomaterials and dynamics of the endosomal maturation processes, enabling a comprehensive analysis of DNA-SWCNT trafficking in the context of the endosomal pathway. The fluorescence and Raman spectra from whole cells were first examined, revealing an increase of fluorescence and G-band intensities from 0 to 6 h of equal magnitude. At the same time, intensity changes from fluorescence emission bands suggested the occurrence of EET between closely packed DNA-SWCNT chiralities. Although the extent of EET plateaued at 6 h, direct aggregation of internalized DNA-SWCNTs was indicated by changes in RBM band intensities, which monotonically scaled with incubation time. To confirm these events were induced by progression of the intracellular trafficking pathway, cells were treated with two pharmacological inhibitors of vesicle maturation, both of which suppressed the identified spectral changes over 6 h via distinct mechanisms of action.

We developed a segmentation process which could colocalize the Raman and fluorescence spectrum of internalized DNA— SWCNTs within nanoscale regions. A simultaneous multipeak fitting algorithm, which provided single-chirality resolution of multicomponent spectra, was used to quantify the relevant spectral features and characterize the conditions of each cellular ROI. This approach determined correlations between fluorescence intensity, DNA-SWCNT concentration, fluorescence emission wavelength, and aggregate formation within cellular ROIs, illustrating the effect of changing intracellular conditions on the internalized DNA-SWCNTs. Immunofluorescence markers for specific endosomal vesicles were applied and colocalized with DNA-SWCNT Raman spectra, enabling spectral signatures to be directly observed from nanotubes encapsulated by specific organelles. Significant colocalization with lysosomal markers confirmed temporal accumulation of DNA-SWCNTs, while colocalized spectral data implicated lysosomes in the irreversible aggregation observed between bare nanotube surfaces, presumably an effect of the catabolic environmental conditions.

Finally, we trained a machine learning algorithm to predict endocytic vesicle type using the Raman spectrum of DNA-SWCNTs contained within. ROIs from nonlabeled hyperspectral data sets were classified to one of three endocytic organelles and endosomal maps were constructed, enabling major components in the endocytic pathway to be simultaneously visualized in whole cells. Additionally, SWCNT fluorescence properties were examined across the modelclassified endosomal vesicles and interpreted with respect to known luminal conditions, thereby relating the endosomal maturation process with the observed spectral dynamics. The approaches detailed in this study could be extrapolated to investigate multiple aspects of ENM-cell interactions. We envision that the spectral immunofluorescence colocalization assay, for example, could be adapted to study intracellular dynamics of other types of ENMs, including the multitude of surface enhanced Raman scattering (SERS) reporters designed for advanced biological applications. Furthermore, this work demonstrates the potential of machine learning techniques for data classification at the single-organelle level, providing a versatile framework to connect multivariate data from complex biological systems.

MATERIALS AND METHODS

DNA–SWCNT Sample Preparation. Raw single-walled carbon nanotubes produced by the HiPco process (Nanointegris) were used throughout this study. For each dispersion, 2 mg of $(GT)_6$ or $(GT)_{30}$ oligonucleotide (Integrated DNA Technologies) was added to 1 mg of raw nanotubes, suspended in 1 mL of 0.1 M NaCl (Sigma-Aldrich), and ultrasonicated using a 1/8 in. tapered microtip for 30 min at 40% amplitude (Sonics Vibracell VCX-130; Sonics and Materials). The resultant suspensions were ultracentrifuged (Sorvall Discovery M120 SE) for 30 min at 250000g and the top \sim 80% of the supernatant was collected. Concentrations were determined using a UV/vis/NIR spectrophotometer (JASCO, Tokyo, Japan) and the extinction coefficient of $A_{910}=0.02554$ L mg $^{-1}$ cm $^{-1}$.

Cell Culture. HUVEC cells (ATCC, Manassas, VA) were cultured under standard incubation conditions at 37 °C and 5% CO $_2$ in endothelial growth media (EGM BulletKit CC-3124, Lonza). For all imaging experiments, cells were seeded into grid labeled collagencoated 35 mm glass bottom microwell dishes (MatTek) to a final concentration of 5,000 cells/cm 2 and allowed to culture for at least 48 h, with regular media replacement every 24 h. To dose the cells, the media was removed from each culture dish, replaced with 1 mg-L $^{-1}$ (GT) $_6$ -SWCNT or (GT) $_{30}$ -SWCNT diluted in media, 20 and incubated for 1 h to allow internalization into the cells. The SWCNT-containing media was removed, the cells were rinsed 3× with sterile phosphate buffered saline (PBS, Gibco), and fresh media was replenished. The 0 h samples were immediately fixed using 4% paraformaldehyde in PBS for 10 min,

rinsed 3× with PBS, and covered with PBS to retain an aqueous environment during imaging. The 3, 6, and 24 h samples were later fixed using the same procedure.

Near-Infrared Fluorescence Microscopy. A near-infrared hyper-spectral fluorescence microscope, similar to a previously described system, ⁵⁶ was used to obtain the hyperspectral fluorescence images from fixed cell samples. Briefly, a continuous 730 nm diode laser with 1.5 W output power was injected into a multimode fiber to produce an excitation source, which was reflected on the sample stage of an Olympus IX-73 inverted microscope equipped with a UApo N 100× /1.49 oil immersion IR objective (Olympus, USA). Emission was passed through a volume Bragg Grating and collected with a 2D InGaAs array detector (Photon Etc.) to generate spectral image stacks. Fixed cell samples were mounted on the hyperspectral microscope to obtain transmitted light images and hyperspectral images from internalized DNA–SWCNTs in individual cells at each time point. Hyperspectral data were processed and extracted using custom codes written with Matlab software.

Confocal Raman Microscopy. Each cell sample was imaged with an inverted WiTec Alpha300 R confocal-Raman microscope (WiTec, Germany) equipped with a Zeiss Epiplan-Neofluar Pol Oil $100\times/1.3$ objective, a 785 nm laser source set to 35 mW sample power, and collected with a UHTS 300 spectrograph (600 lines/mm grating) coupled with an Andor DR32400 CCD detector (-61 °C, 1650×200 pixels). Small cellular areas were scanned, and spectra were obtained in $0.29\times0.29~\mu{\rm m}$ intervals using 0.2 s integration time per spectrum to construct hyperspectral images of individual cells. Global background subtraction and cosmic-ray removal were performed on each scan using Witec Project 5.2 software. Hyperspectral data was extracted and processed using custom codes written with Matlab software.

Pharmacological Inhibition of Endosomal Maturation. HUVEC cells were cultured and dosed with $(GT)_6$ -SWCNTs or $(GT)_{30}$ -SWCNTs following the same procedure previously described; however, the media used to replenish the cells after DNA–SWCNT removal and PBS rinsing was spiked with 10 μ g mL⁻¹ nocodazole (NOC) or 100 μ M chloroquine (CQ). The cells were incubated for 6 h following the addition of inhibitors before fixation in 4% paraformaldehyde in PBS for 10 min. The cells were then imaged following the same procedure used for the untreated cells.

ROI Colocalization. ROI colocalization was carried out on all hyperspectral "cubes" (i.e., three-dimensional data sets in which x and ydimensions are spatial coordinates, the z dimension is the spectral coordinate, and the pixel value corresponds to the spectral intensity) following initial background subtraction and cosmic-ray removal steps. Using custom Matlab codes, composite fluorescence images were created by integrating the entire spectral dimension and composite Raman images were created by integrating the G-band or RBM regions of the spectrum. The fluorescence and Raman images were first roughly colocalized by applying an intensity threshold to each image, binarizing and segmenting each image individually, determining the intensityweighted centroid of each segmented ROI, and iteratively overlaying the images to find the coordinates which minimize the root-meansquare deviation (RMSD) of similar ROIs. Next, the composite images and cubes were cropped and imported to the open-source image processing software FIJI. The G-band composite images were segmented into ROIs, which were manually adjusted to ensure consistency in the segmentation process, and compared with the RBM region of the Raman cube. The ROIs determined from the Raman data were then transferred to the fluorescence images, where each ROI was manually adjusted to account for minor discrepancies in their location and shape. Once all ROIs were determined for a cell, their locations were imported to Matlab for further analysis. Of note, the resolution of the confocal Raman area scans was experimentally optimized prior to data acquisition to match the pixel size of the hyperspectral fluorescence microscope, and thus, the spatial resolution of the two cubes was essentially the same. ROI location adjustments mainly accounted for minor rotations of the imaging field as the result of mounting on two separate instruments, and ROIs which could not be clearly identified as the same were disregarded. In certain cases, ROIs which exhibited strong Raman intensities in both the G-band and RBM

regions displayed little to no fluorescence intensity from the same spatial location. These ROIs were considered to be colocalized and accurate only if their G-band and RBM integrated intensities were comparable with other ROIs in the same image and other nearby ROIs which exhibited fluorescence were colocalized with Raman signal. The appearance of visible, dark spots within these ROIs in transmitted light images obtained with the hyperspectral fluorescence microscope were also used to verify the presence of DNA–SWCNTs which were quenched. An example of quenched fluorescence from cellular ROIs is provided in the Supporting Information. Any and all ROIs which could not be definitively colocalized were disregarded from further data analysis.

Multi-Peak Fitting of the Fluorescence and RBM Spectra. The colocalized ROI data for the fluorescence and Raman cubes were used to obtain average spectra from each ROI, which was processed with a custom Matlab pipeline. First, the average fluorescence and Raman spectra from each ROI were calculated by averaging pixel intensity values in their x-y direction and extracting the spectral z dimension from each cube. The fluorescence spectrum from each ROI was fitted to an additive combination of Voigt line shapes corresponding to the single chirality component spectra, and only chiralities which were identified to significantly contribute to the fluorescence spectrum were included in the fitting process. The peak center wavelength and width parameters of each chirality were allowed to vary independently, but each parameter was limited within the same set of constraints. The area under the curve and global offset were restricted to non-negative values. The radial breathing mode of the Raman spectrum in each ROI was fit to an additive combination of Lorentz line shapes corresponding to the single chirality component spectra. The chiralities which were included in the fits were chosen based on (1) their resonance with the excitation laser, determined by empirical Katura plots found in the literature, ⁴⁹ (2) their presence when spectra were obtained from solution controls, and (3) their presence when spectra were obtained from aggregated samples. Peak centers were initially specified and allowed to shift within a very small window; however, each spectrum was restricted to a single full width at half-maximum for all peaks. 57 The area under the curve and global offset were restricted to non-negative values. $r^2 > 0.95$ was used as a cutoff to remove poor-fitting ROI data from further analyses.

Primary and Secondary Antibodies. Rabbit anti-EEA1 (no. MA5-14794), rabbit anti-Rab7 (no. PA5-52369), and rabbit anti-Rab11a (no. 71-5300) primary antibodies and goat antirabbit IgG Alexa Fluor 532 (no. A-11009) secondary antibodies were purchased from Thermo Fisher Scientific (Waltham, MA). Rabbit anti-LAMP1 (no. ab24170) was purchased from Abcam (Cambridge, MA).

Immunofluorescence Staining Procedures. HUVEC cells were cultured and dosed with (GT)₃₀-SWCNTs using the same procedure previously described. Two separate protocols were used for immunofluorescence staining procedures. (1) Samples stained against EEA1, RAB7, and RAB11a were fixed with 4% PFA for 15 min and rinsed three times with PBS. Cells were permeabilized and blocked with a saturation solution (PBS; 10% goat serum (Gibco); 0.05% saponin) for 45 min. Primary antibodies, diluted in saturation solution (1:200), were allowed to incubate overnight while kept in a humid container at 4 °C, after which samples were thoroughly washed in PBS and allowed to sit for 5 min. Cells were subsequently incubated with secondary antibodies, diluted in PBS (1:1000), for 30 min at room temperature, washed three times with PBS, and covered with a layer of PBS throughout imaging. (2) Samples stained against LAMP1 were fixed with -20 °C methanol for 5 min and washed multiple times in PBS. The first rinse was added before methanol removal to prevent rapid dehydration, and the final rinse was allowed to sit for 5 min. Samples were incubated in blocking buffer (PBS; 10% goat serum) for 45 min. Primary antibodies, diluted in blocking buffer (1:200), were allowed to incubate overnight while kept in a humid container at 4 $^{\circ}\text{C}\text{,}$ after which samples were thoroughly washed in PBS and allowed to sit for 5 min. Cells were subsequently incubated with secondary antibodies, diluted in PBS (1:1000), for 30 min at room temperature, washed three times with PBS, and covered with a layer of PBS throughout imaging.

Immunofluorescence Data Acquisition. Samples were imaged with an inverted WiTec Alpha300 R confocal-Raman microscope

(WiTec, Germany) equipped with a Zeiss Epiplan-Neofluar Pol Oil $100\times/1.3$ objective. Single cells were scanned in $0.25\times0.25~\mu\mathrm{m}$ intervals using a 532 nm laser source set to $10~\mu\mathrm{W}$ sample power to collect confocal fluorescence data. The same region was immediately rescanned using a 785 nm laser source set to 35 mW sample power to collect confocal Raman data. We accounted for chromatic aberration by applying a predetermined offset in the z-direction between scans. The offset was acquired from a series of depth scans on silicon substrates, in which the intensity profile of a reference peak was compared and matched between 532 and 785 nm spectra in the z-direction. Global background subtraction and cosmic-ray removal were performed on each scan using Witec Project 5.2 software. Hyperspectral data was extracted and processed using custom codes written with Matlab software.

Immunofluorescence Image Processing. Raw fluorescence images were constructed from immunofluorescence hyperspectral data sets by calculating the total spectral intensity from all data points between 300 cm⁻¹ (\sim 540 nm) and 1350 cm⁻¹ (\sim 570 nm). The following processes were then applied to create binary fluorescence images. Note that specific intensity values, morphological operation values, etc., were globally applied to images from the same immunofluorescence marker; however, each stain was optimized independently. A global intensity value was subtracted to remove background signal and a top hat filter was applied to remove objects much larger than the organelles from the images. Next, a global threshold was applied to create binary fluorescence images. A watershed transform was performed to divide individual organelle structures, and finally binary image opening was applied to create binary fluorescence representations of each organelle label. DNA-SWCNT Raman images were constructed from confocal Raman hyperspectral data sets by calculating the total spectral intensity from all data points between 200 and 300 cm⁻¹. The following processes were then applied to create binary DNA-SWCNT images, and the same global settings were used regardless of the corresponding immunofluorescence marker. A global threshold was applied to create binary images and remove background signal. A watershed transform was initially performed to divide large DNA-SWCNT-containing regions. Binary erosion was used to shrink connections between regions of separate ROIs in close proximity, and a second watershed transform was applied to completely separate close ROIs which could not be initially distinguished. Finally, each DNA-SWCNT ROI was given a label before proceeding to the colocalization analysis. All images were constructed using custom Matlab codes and binary image operations were performed with FIJI.

Quantitative Colocalization Analysis. Colocalization analysis was performed by assessing each DNA–SWCNT ROI independently with respect to the corresponding binary fluorescence image. The intensity-weighted centroid position was calculated for a given ROI using the intensity image pixel values. The DNA–SWCNT ROI was then considered to colocalize with the immunofluorescence labels if the following conditions were met. (1) The intensity-weighted centroid position overlapped with the fluorescence binary image within a 1.5-pixel radius. (2) Greater than 40% of the total ROI pixels overlapped with fluorescence binary pixels. The first condition ensured that the DNA–SWCNT intensity-center was within a resolvable distance of the fluorescence objects, ⁶⁸ while the second condition essentially applied a colocalization percentage threshold. ⁶⁹ All colocalization analyses were performed using custom Matlab codes.

Development of Artificial Neural Network. An artificial neural network classification model was developed, trained, and implemented using built-in functions and models from the Matlab Statistics and Machine Learning Toolbox. The training data set was compiled from DNA–SWCNT Raman spectra of ROIs which colocalized with early endosome, late endosome, or lysosome markers at 0, 6, or 24 h time points, respectively. We chose to only include data from the time point with the highest degree of colocalization for each marker as a way to reduce the potential for overlap between the protein labels, therefore training the neural network with the best representative spectra for each organelle. Additionally, recycling endosome data was omitted due to a lack of observations and considerable similarities to the early endosome spectra. As a preprocessing step, principle component analysis (PCA)

was applied to the input Raman spectra to reduce the spectrum dimensionality and help prevent overfitting. The final number of inputs per spectrum was reduced to 44 components, comprised of the PCA components which explained 95% of variance within the entire training data set. The artificial neural network was comprised of an input layer connecting to the training predictor data set, two fully connected 25node hidden layers activated by rectified linear unit (ReLU) functions, and a softmax layer to convert the previous layer output into a class probability distribution. Layer weights and biases were established by the training data set, and the model was validated with a 10-fold crossvalidation. The model was applied to classify the Raman spectra of all nonlabeled (GT)₃₀-SWCNT ROI data. Each input spectrum was transformed by PCA using the same parameters from the training data set and input to the model for classification. The resulting output consisted of the predicted class label and the probability distribution corresponding to each class.

Statistical Analysis. OriginPro 2018 was used to perform all statistical analysis. All data either met assumptions of the statistical tests performed (*i.e.*, normality, equal variances, *etc.*) or was transformed to meet assumptions before statistical analysis was carried out. Statistical significance was analyzed using two-sample two-tailed student *t* test or one-way ANOVA where appropriate. Testing of multiple hypotheses was accounted for by performing one-way ANOVA with Tukey's post hoc test. Specific information about statistical analyses can be found in figure legends.

ASSOCIATED CONTENT

Supporting Information

The Supporting Information is available free of charge at https://pubs.acs.org/doi/10.1021/acsnano.1c04500.

Additional figures of DNA–SWCNT optical characterization, intracellular $(\mathrm{GT})_6$ -SWCNT data, subcellular pharmacological inhibitor data, ROI analysis using (8,6)-SWCNTs, quenched DNA–SWCNT fluorescence example, immunofluorescence control images and colocalization example, Raman spectra from DNA–SWCNTs in stained organelles, DNA–SWCNT fluorescence controls, neural network validation figures and table, table with optical properties of relevant SWCNT chiralities (PDF)

AUTHOR INFORMATION

Corresponding Author

Daniel Roxbury — Department of Chemical Engineering, University of Rhode Island, Kingston, Rhode Island 02881, United States; orcid.org/0000-0003-2812-3523; Email: roxbury@uri.edu

Author

Mitchell Gravely — Department of Chemical Engineering, University of Rhode Island, Kingston, Rhode Island 02881, United States; orcid.org/0000-0001-7938-6054

Complete contact information is available at: https://pubs.acs.org/10.1021/acsnano.1c04500

Note:

A preprint of this work has been submitted to the bioRxiv repository: Gravely, M.; Roxbury, D. Multispectral Finger-printing Resolves Dynamics of Nanomaterial Trafficking in Primary Endothelial Cells. *bioRxiv*, 2020, 10.1101/2020.12.14. 422763. (accessed 2020-12-15).

The authors declare no competing financial interest.

ACKNOWLEDGMENTS

This work was supported by National Science Foundation CAREER Award No. 1844536. The confocal Raman data was

acquired at the RI Consortium for Nanoscience and Nanotechnology, a URI College of Engineering core facility partially funded by the National Science Foundation EPSCoR, Cooperative Agreement No. OIA-1655221. We acknowledge and thank P. V. Jena for the Matlab codes which were adapted to become a part of the full data processing pipeline.

REFERENCES

- (1) Conner, S. D.; Schmid, S. L. Regulated Portals of Entry into the Cell. *Nature* **2003**, 422, 37–44.
- (2) Rink, J.; Ghigo, E.; Kalaidzidis, Y.; Zerial, M. Rab Conversion as a Mechanism of Progression from Early to Late Endosomes. *Cell* **2005**, 122, 735–749.
- (3) Huotari, J.; Helenius, A. Endosome Maturation. *EMBO J.* **2011**, 30, 3481–3500.
- (4) Oh, N.; Park, J.-H. Endocytosis and Exocytosis of Nanoparticles in Mammalian Cells. *Int. J. Nanomed.* **2014**, *9*, 51.
- (5) Jena, P. V.; Roxbury, D.; Galassi, T. V.; Akkari, L.; Horoszko, C. P.; Iaea, D. B.; Budhathoki-Uprety, J.; Pipalia, N.; Haka, A. S.; Harvey, J. D. A Carbon Nanotube Optical Reporter Maps Endolysosomal Lipid Flux. *ACS Nano* **2017**, *11*, 10689–10703.
- (6) Xu, H.; Ren, D. Lysosomal Physiology. *Annu. Rev. Physiol.* **2015**, 77, 57–80.
- (7) Donahue, N. D.; Acar, H.; Wilhelm, S. Concepts of Nanoparticle Cellular Uptake, Intracellular Trafficking, and Kinetics in Nanomedicine. *Adv. Drug Delivery Rev.* **2019**, *143*, 68–96.
- (8) Chithrani, B. D.; Ghazani, A. A.; Chan, W. C. Determining the Size and Shape Dependence of Gold Nanoparticle Uptake into Mammalian Cells. *Nano Lett.* **2006**, *6*, 662–668.
- (9) Dasgupta, S.; Auth, T.; Gompper, G. Shape and Orientation Matter for the Cellular Uptake of Nonspherical Particles. *Nano Lett.* **2014**, *14*, 687–693.
- (10) Zhu, M.; Nie, G.; Meng, H.; Xia, T.; Nel, A.; Zhao, Y. Physicochemical Properties Determine Nanomaterial Cellular Uptake, Transport, and Fate. *Acc. Chem. Res.* **2013**, *46*, 622–631.
- (11) Walkey, C. D.; Olsen, J. B.; Guo, H.; Emili, A.; Chan, W. C. Nanoparticle Size and Surface Chemistry Determine Serum Protein Adsorption and Macrophage Uptake. *J. Am. Chem. Soc.* **2012**, *134*, 2139–2147.
- (12) Pinals, R. L.; Yang, D.; Rosenberg, D. J.; Chaudhary, T.; Crothers, A. R.; Iavarone, A. T.; Hammel, M.; Landry, M. P. Quantitative Protein Corona Composition and Dynamics on Carbon Nanotubes in Biological Environments. *Angew. Chem.* **2020**, *132*, 23876–23885.
- (13) Nixon, R. A. Endosome Function and Dysfunction in Alzheimer's Disease and Other Neurodegenerative Diseases. *Neurobiol. Aging* **2005**, 26, 373–382.
- (14) Fukuda, T.; Ewan, L.; Bauer, M.; Mattaliano, R. J.; Zaal, K.; Ralston, E.; Plotz, P. H.; Raben, N. Dysfunction of Endocytic and Autophagic Pathways in a Lysosomal Storage Disease. *Ann. Neurol.* **2006**, *59*, 700–708.
- (15) Sarkar, S.; Carroll, B.; Buganim, Y.; Maetzel, D.; Ng, A. H.; Cassady, J. P.; Cohen, M. A.; Chakraborty, S.; Wang, H.; Spooner, E. Impaired Autophagy in the Lipid-Storage Disorder Niemann-Pick Type C1 Disease. *Cell Rep.* **2013**, *5*, 1302–1315.
- (16) Mercer, J.; Schelhaas, M.; Helenius, A. Virus Entry by Endocytosis. *Annu. Rev. Biochem.* **2010**, *79*, 803–833.
- (17) Sandin, P.; Fitzpatrick, L. W.; Simpson, J. C.; Dawson, K. A. High-Speed Imaging of Rab Family Small GTPases Reveals Rare Events in Nanoparticle Trafficking in Living Cells. *ACS Nano* **2012**, *6*, 1513–1521.
- (18) Vercauteren, D.; Deschout, H.; Remaut, K.; Engbersen, J. F.; Jones, A. T.; Demeester, J.; De Smedt, S. C.; Braeckmans, K. Dynamic Colocalization Microscopy to Characterize Intracellular Trafficking of Nanomedicines. *ACS Nano* **2011**, *5*, 7874–7884.
- (19) Galassi, T. V.; Jena, P. V.; Shah, J.; Ao, G.; Molitor, E.; Bram, Y.; Frankel, A.; Park, J.; Jessurun, J.; Ory, D. S. An Optical Nanoreporter of

- Endolysosomal Lipid Accumulation Reveals Enduring Effects of Diet on Hepatic Macrophages in Vivo. Sci. Transl. Med. 2018, 10, eaar2680.
- (20) Gravely, M.; Safaee, M. M.; Roxbury, D. Biomolecular Functionalization of a Nanomaterial to Control Stability and Retention within Live Cells. *Nano Lett.* **2019**, *19*, 6203–6212.
- (21) Jin, S.; Wijesekara, P.; Boyer, P. D.; Dahl, K. N.; Islam, M. F. Length-Dependent Intracellular Bundling of Single-Walled Carbon Nanotubes Influences Retention. *J. Mater. Chem. B* **2017**, *5*, 6657–6665
- (22) Kneipp, J.; Kneipp, H.; Wittig, B.; Kneipp, K. Following the Dynamics of pH in Endosomes of Live Cells with SERS Nanosensors. *J. Phys. Chem. C* **2010**, *114*, 7421–7426.
- (23) Huefner, A.; Kuan, W.-L.; Müller, K. H.; Skepper, J. N.; Barker, R. A.; Mahajan, S. Characterization and Visualization of Vesicles in the Endo-Lysosomal Pathway with Surface-Enhanced Raman Spectroscopy and Chemometrics. *ACS Nano* **2016**, *10*, 307–316.
- (24) Gowen, A. A.; O'Donnell, C. P.; Cullen, P. J.; Downey, G.; Frias, J. M. Hyperspectral Imaging—An Emerging Process Analytical Tool for Food Quality and Safety Control. *Trends Food Sci. Technol.* **2007**, *18*, 590–598.
- (25) Jorio, A.; Fantini, C.; Pimenta, M.; Heller, D.; Strano, M.; Dresselhaus, M.; Oyama, Y.; Jiang, J.; Saito, R. Carbon Nanotube Population Analysis from Raman and Photoluminescence Intensities. *Appl. Phys. Lett.* **2006**, *88*, 023109.
- (26) Ebbesen, T.; Lezec, H.; Hiura, H.; Bennett, J.; Ghaemi, H.; Thio, T. Electrical Conductivity of Individual Carbon Nanotubes. *Nature* **1996**, 382, 54–56.
- (27) Bachilo, S. M.; Strano, M. S.; Kittrell, C.; Hauge, R. H.; Smalley, R. E.; Weisman, R. B. Structure-Assigned Optical Spectra of Single-Walled Carbon Nanotubes. *Science* **2002**, *298*, 2361–2366.
- (28) Jorio, A.; Pimenta, M.; Souza Filho, A.; Saito, R.; Dresselhaus, G.; Dresselhaus, M. Characterizing Carbon Nanotube Samples with Resonance Raman Scattering. *New J. Phys.* **2003**, *5*, 139.
- (29) O'connell, M. J.; Bachilo, S. M.; Huffman, C. B.; Moore, V. C.; Strano, M. S.; Haroz, E. H.; Rialon, K. L.; Boul, P. J.; Noon, W. H.; Kittrell, C. Band Gap Fluorescence from Individual Single-Walled Carbon Nanotubes. *Science* **2002**, *297*, 593–596.
- (30) Liu, Z.; Davis, C.; Cai, W.; He, L.; Chen, X.; Dai, H. Circulation and Long-Term Fate of Functionalized, Biocompatible Single-Walled Carbon Nanotubes in Mice Probed by Raman Spectroscopy. *Proc. Natl. Acad. Sci. U. S. A.* **2008**, *105*, 1410–1415.
- (31) Heller, D. A.; Barone, P. W.; Swanson, J. P.; Mayrhofer, R. M.; Strano, M. S. Using Raman Spectroscopy to Elucidate the Aggregation State of Single-Walled Carbon Nanotubes. *J. Phys. Chem. B* **2004**, *108*, 6905–6909.
- (32) Brown, S.; Jorio, A.; Dresselhaus, M.; Dresselhaus, G. Observations of the D-Band Feature in the Raman Spectra of Carbon Nanotubes. *Phys. Rev. B: Condens. Matter Mater. Phys.* **2001**, *64*, 073403.
- (33) Smith, A. M.; Mancini, M. C.; Nie, S. Second Window for *in Vivo* Imaging. *Nat. Nanotechnol.* **2009**, *4*, 710–711.
- (34) Choi, J. H.; Strano, M. S. Solvatochromism in Single-Walled Carbon Nanotubes. *Appl. Phys. Lett.* **2007**, *90*, 223114.
- (35) Heller, D. A.; Pratt, G. W.; Zhang, J.; Nair, N.; Hansborough, A. J.; Boghossian, A. A.; Reuel, N. F.; Barone, P. W.; Strano, M. S. Peptide Secondary Structure Modulates Single-Walled Carbon Nanotube Fluorescence As a Chaperone Sensor for Nitroaromatics. *Proc. Natl. Acad. Sci. U. S. A.* **2011**, *108*, 8544–8549.
- (36) Roxbury, D.; Jena, P. V.; Shamay, Y.; Horoszko, C. P.; Heller, D. A. Cell Membrane Proteins Modulate the Carbon Nanotube Optical Bandgap *via* Surface Charge Accumulation. *ACS Nano* **2016**, *10*, 499–506.
- (37) Barone, P. W.; Strano, M. S. Reversible Control of Carbon Nanotube Aggregation for a Glucose Affinity Sensor. *Angew. Chem.* **2006**, *118*, 8318–8321.
- (38) Gillen, A. J.; Kupis-Rozmysłowicz, J.; Gigli, C.; Schuergers, N.; Boghossian, A. A. Xeno Nucleic Acid Nanosensors for Enhanced Stability against Ion-Induced Perturbations. *J. Phys. Chem. Lett.* **2018**, *9*, 4336–4343.

- (39) Safaee, M. M.; Gravely, M.; Roxbury, D. A Wearable Optical Microfibrous Biomaterial with Encapsulated Nanosensors Enables Wireless Monitoring of Oxidative Stress. *Adv. Funct. Mater.* **2021**, *31*, 2006254.
- (40) Zheng, M.; Jagota, A.; Semke, E. D.; Diner, B. A.; McLean, R. S.; Lustig, S. R.; Richardson, R. E.; Tassi, N. G. DNA-Assisted Dispersion and Separation of Carbon Nanotubes. *Nat. Mater.* **2003**, *2*, 338–342.
- (41) Gao, Z.; Varela, J. A.; Groc, L.; Lounis, B.; Cognet, L. Toward the Suppression of Cellular Toxicity from Single-Walled Carbon Nanotubes. *Biomater. Sci.* **2016**, *4*, 230–244.
- (42) Boghossian, A. A.; Zhang, J.; Barone, P. W.; Reuel, N. F.; Kim, J. H.; Heller, D. A.; Ahn, J. H.; Hilmer, A. J.; Rwei, A.; Arkalgud, J. R. Near-Infrared Fluorescent Sensors Based on Single-Walled Carbon Nanotubes for Life Sciences Applications. *ChemSusChem* **2011**, *4*, 848.
- (43) Budhathoki-Uprety, J.; Jena, P. V.; Roxbury, D.; Heller, D. A. Helical Polycarbodiimide Cloaking of Carbon Nanotubes Enables Inter-Nanotube Exciton Energy Transfer Modulation. *J. Am. Chem. Soc.* **2014**, *136*, 15545–15550.
- (44) Safaee, M. M.; Gravely, M.; Rocchio, C.; Simmeth, M.; Roxbury, D. DNA Sequence Mediates Apparent Length Distribution in Single-Walled Carbon Nanotubes. ACS Appl. Mater. Interfaces 2019, 11, 2225–2233.
- (45) Jena, P. V.; Safaee, M. M.; Heller, D. A.; Roxbury, D. DNA—Carbon Nanotube Complexation Affinity and Photoluminescence Modulation Are Independent. *ACS Appl. Mater. Interfaces* **2017**, *9*, 21397—21405.
- (46) Ferrari, A. C.; Robertson, J. Interpretation of Raman Spectra of Disordered and Amorphous Carbon. *Phys. Rev. B: Condens. Matter Mater. Phys.* **2000**, *61*, 14095.
- (47) Park, H.-J.; Zhang, Y.; Georgescu, S. P.; Johnson, K. L.; Kong, D.; Galper, J. B. Human Umbilical Vein Endothelial Cells and Human Dermal Microvascular Endothelial Cells Offer New Insights into the Relationship between Lipid Metabolism and Angiogenesis. *Stem Cell Rev.* **2006**, *2*, 93–101.
- (48) Torrens, O.; Milkie, D.; Zheng, M.; Kikkawa, J. Photoluminescence from Intertube Carrier Migration in Single-Walled Carbon Nanotube Bundles. *Nano Lett.* **2006**, *6*, 2864–2867.
- (49) Weisman, R. B.; Bachilo, S. M. Dependence of Optical Transition Energies on Structure for Single-Walled Carbon Nanotubes in Aqueous Suspension: An Empirical Kataura Plot. *Nano Lett.* **2003**, *3*, 1235–1238.
- (50) Reich, S.; Dworzak, M.; Hoffmann, A.; Thomsen, C.; Strano, M. Excited-State Carrier Lifetime in Single-Walled Carbon Nanotubes. *Phys. Rev. B: Condens. Matter Mater. Phys.* **2005**, *71*, 033402.
- (51) Crochet, J.; Clemens, M.; Hertel, T. Quantum Yield Heterogeneities of Aqueous Single-Wall Carbon Nanotube Suspensions. J. Am. Chem. Soc. 2007, 129, 8058–8059.
- (52) Bayer, N.; Schober, D.; Prchla, E.; Murphy, R. F.; Blaas, D.; Fuchs, R. Effect of Bafilomycin A1 and Nocodazole on Endocytic Transport in HeLa Cells: Implications for Viral Uncoating and Infection. *J. Virol.* **1998**, *72*, 9645–9655.
- (53) Ohkuma, S.; Poole, B. Fluorescence Probe Measurement of the Intralysosomal pH in Living Cells and the Perturbation of pH by Various Agents. *Proc. Natl. Acad. Sci. U. S. A.* **1978**, *75*, 3327–3331.
- (54) Mauthe, M.; Orhon, I.; Rocchi, C.; Zhou, X.; Luhr, M.; Hijlkema, K.-J.; Coppes, R. P.; Engedal, N.; Mari, M.; Reggiori, F. Chloroquine Inhibits Autophagic Flux by Decreasing Autophagosome-Lysosome Fusion. *Autophagy* **2018**, *14*, 1435–1455.
- (55) Mesaki, K.; Tanabe, K.; Obayashi, M.; Oe, N.; Takei, K. Fission of Tubular Endosomes Triggers Endosomal Acidification and Movement. *PLoS One* **2011**, *6*, e19764.
- (56) Roxbury, D.; Jena, P. V.; Williams, R. M.; Enyedi, B.; Niethammer, P.; Marcet, S.; Verhaegen, M.; Blais-Ouellette, S.; Heller, D. A. Hyperspectral Microscopy of Near-Infrared Fluorescence Enables 17-Chirality Carbon Nanotube Imaging. *Sci. Rep.* **2015**, *S*, 1–6. (57) Araujo, P.; Pesce, P.; Dresselhaus, M.; Sato, K.; Saito, R.; Jorio, A. Resonance Raman Spectroscopy of the Radial Breathing Modes in Carbon Nanotubes. *Phys. E* **2010**, *42*, 1251–1261.

- (58) Heller, D. A.; Jeng, E. S.; Yeung, T.-K.; Martinez, B. M.; Moll, A. E.; Gastala, J. B.; Strano, M. S. Optical Detection of DNA Conformational Polymorphism on Single-Walled Carbon Nanotubes. *Science* **2006**, *311*, 508–511.
- (59) Fantini, C.; Jorio, A.; Souza, M.; Strano, M.; Dresselhaus, M.; Pimenta, M. Optical Transition Energies for Carbon Nanotubes from Resonant Raman Spectroscopy: Environment and Temperature Effects. *Phys. Rev. Lett.* **2004**, 93, 147406.
- (60) Mu, F.-T.; Callaghan, J. M.; Steele-Mortimer, O.; Stenmark, H.; Parton, R. G.; Campbell, P. L.; McCluskey, J.; Yeo, J.-P.; Tock, E. P.; Toh, B.-H. EEA1, an Early Endosome-Associated Protein.: EEA1 Is a Conserved Alpha-Helical Peripheral Membrane Protein Flanked by Cysteine "Fingers" and Contains a Calmodulin-Binding IQ Motif. *J. Biol. Chem.* 1995, 270, 13503–13511.
- (61) Bottger, G.; Nagelkerken, B.; van der Sluijs, P. Rab4 and Rab7 Define Distinct Nonoverlapping Endosomal Compartments. *J. Biol. Chem.* **1996**, 271, 29191–29197.
- (62) Ullrich, O.; Reinsch, S.; Urbé, S.; Zerial, M.; Parton, R. G. Rab11 Regulates Recycling through the Pericentriolar Recycling Endosome. *J. Cell Biol.* **1996**, *135*, 913–924.
- (63) Kornfeld, S.; Mellman, I. The Biogenesis of Lysosomes. *Annu. Rev. Cell Biol.* **1989**, *5*, 483–525.
- (64) Saftig, P.; Klumperman, J. Lysosome Biogenesis and Lysosomal Membrane Proteins: Trafficking Meets Function. *Nat. Rev. Mol. Cell Biol.* **2009**, *10*, 623–635.
- (65) Abiodun, O. I.; Jantan, A.; Omolara, A. E.; Dada, K. V.; Mohamed, N. A.; Arshad, H. State-of-the-Art in Artificial Neural Network Applications: A Survey. *Heliyon* **2018**, *4*, e00938.
- (66) Scott, C. C.; Gruenberg, J. Ion Flux and the Function of Endosomes and Lysosomes: pH is Just the Start: The Flux of Ions across Endosomal Membranes Influences Endosome Function Not Only through Regulation of the Luminal pH. *BioEssays* **2011**, 33, 103–110
- (67) Thelen, A. M.; Zoncu, R. Emerging Roles for the Lysosome in Lipid Metabolism. *Trends Cell Biol.* **2017**, 27, 833–850.
- (68) Bolte, S.; Cordelières, F. P. A Guided Tour into Subcellular Colocalization Analysis in Light Microscopy. *J. Microsc.* **2006**, 224, 213–232.
- (69) Gilleron, J.; Querbes, W.; Zeigerer, A.; Borodovsky, A.; Marsico, G.; Schubert, U.; Manygoats, K.; Seifert, S.; Andree, C.; Stöter, M. Image-Based Analysis of Lipid Nanoparticle–Mediated siRNA Delivery, Intracellular Trafficking and Endosomal Escape. *Nat. Biotechnol.* **2013**, *31*, 638–646.